Gezamenlijke opleiding UHasselt en KU Leuven

2018•2019
Faculteit Industriële ingenieurswetenschappen
master in de industriële wetenschappen: elektronica-ICT

Masterthesis

Potential-Induced Degradation of photovoltaic modules: an automated approach

PROMOTOR :
Prof. dr. ir. Michael DAENEN

PROMOTOR :
Dhr. Marc MEURIS

BEGELEIDER :
ing. Jorne CAROLUS

Jonathan Luijsmans, Melissa Struys

Scriptie ingediend tot het behalen van de graad van master in de industriële wetenschappen: elektronica-ICT

2018•2019
Faculteit Industriële ingenieurswetenschappen
master in de industriële wetenschappen: elektronica-ICT

Masterthesis

Potential-Induced Degradation of photovoltaic modules: an automated approach

PROMOTOR :
Prof. dr. ir. Michael DAENEN

PROMOTOR :
Dhr. Marc MEURIS

BEGELEIDER :
ing. Jorne CAROLUS

Jonathan Luijsmans, Melissa Struys

Scriptie ingediend tot het behalen van de graad van master in de industriële wetenschappen: elektronica-ICT

KU LEUVEN

Acknowledgements

This Master's thesis is the summit of our education to Master of Science in Electronics and ICT Engineering Technology at UHasselt and KU Leuven. The realization of this thesis was a captivating and challenging adventure. It is the result of hard work and perseverance. Therefore, we would like to thank everyone who devoted their time to support us.

In particular, we would like to express our deepest appreciation to our promotor prof. dr. ir. Michaël Daenen and supervisor ing. Jorne Carolus. They provided us with the necessary knowledge and skills. Their guidance helped us when we encountered a problem.

We would like to thank the co-workers of the research group Energy Systems Engineering (ESE) and EnergyVille for their assistance and creating a pleasurable work environment. Furthermore, we would like to thank our fellow master students for the new friendships and support.

A special thanks to our family and friends for supporting us whenever needed. Especially, thanks to our parents for giving us the opportunity to start this study and never stop to believe in us.

Jonathan Luijsmans & Melissa Struys
June 2019

Table of contents

1 INTRODUCTION 15

2 LITERATURE REVIEW 17

2.1 PHOTOVOLTAICS 17
2.1.1 Photovoltaic cells 17
2.1.1.1 Crystalline silicon photovoltaic cells 17
2.1.1.1.1 Mono and multi crystalline silicon photovoltaic cells 17
2.1.1.1.2 Bifacial silicon photovoltaic cells 19
2.1.2 Photovoltaic modules 20
2.1.3 Photovoltaic systems 21
2.2 PHOTOVOLTAIC CHARACTERIZATION 22
2.2.1 PV cell model 22
2.2.2 IV curve 22
2.2.2.1 Light IV 22
2.2.2.2 Dark IV 24
2.2.3 Electroluminescence 24
2.2.4 External quantum efficiency 25
2.2.5 Electron beam induced current 26
2.2.6 Laser beam induced current 26
2.2.7 Dark lock-in thermography 26
2.3 PID OF PHOTOVOLTAICS 27
2.3.1 PID types 27
2.3.1.1 PID of the shunting type (PID-s) 27
2.3.1.2 PID of the polarization type (PID-p) 28
2.3.1.3 PID of the corrosion type (PID-c) 29
2.3.1.4 PID of the delamination type (PID-d) 29
2.3.2 PID stressing methods 29
2.3.2.1 Frame method 29
2.3.2.2 Foil method 30
2.3.2.3 PID tests on cell level 30
2.3.3 PID quantification 31
2.3.3.1 IV-curve 31
2.3.3.1.1 Light IV measurement 31
2.3.3.1.2 Dark IV measurement 32
2.3.3.2 Electroluminescence imaging 34
2.3.3.3 External quantum efficiency 34
2.3.3.4 Electron beam induced current 35
2.3.3.5 Dark lock-in thermography 36
2.3.4 PID kinetics 36
2.3.4.1 Temperature 36
2.3.4.2 Humidity 37
2.3.4.3 Voltage 37
2.3.5 PID preventive measures 37
2.3.5.1 Cell level 37
2.3.5.2 Module level 38
2.3.5.2.1 Glass 38
2.3.5.2.2 Encapsulant material 38
2.3.5.3 System level 39
2.3.6 PID recovery 39
2.3.6.1 Thermal recovery 39
2.3.6.2 Voltage recovery 39
2.3.6.3 Light recovery 40

3 MATERIAL AND METHODS 41

3.1 SOFTWARE 41
3.1.1 LabVIEW 41
3.1.2 Python 41
3.2 HARDWARE 42
3.2.1 PV-tools LOANA 42
3.2.2 EL-camera 42
3.2.3 High voltage source 42
3.2.4 Keithley 2400 43

3.2.5 Climate chamber ... *43*

4 DESIGN RESULTS ... 45

4.1 SWITCH MATRIX ... 45
4.1.1 Setup ... *45*
4.1.2 Photovoltaic characterisation ... *46*
4.1.3 Stress testing ... *46*
4.1.4 Front panel layout ... *47*
4.1.5 Low voltage electrical control ... *47*
4.1.6 Software: LabVIEW ... *48*
4.2 DATA AUTOMATION WITH PYTHON ... 50
4.2.1 Data processing of PV module measurements ... *50*
4.2.1.1 LOANA ... 50
4.2.1.2 PME ... 52
4.2.1.3 K2400 ... 52
4.2.2 Combine EL-photos of PV-laminates ... *53*
4.2.3 Graphical User Interface of data processing program ... *53*

5 PID-S TEST WITH SWITCH MATRIX ... 55

5.1 EXPERIMENTAL ... 55
5.2 RESULTS ... 56
5.3 DISCUSSION AND CONCLUSION ... 64

6 CONCLUSION ... 65

BIBLIOGRAPHY / REFERENCES ... 67

List of tables

Table 5.1: Cell parameters before and after stressing 58
Table 5.2: Cell parameters before stressing, after stressing and after curing 63

List of figures

Figure 1.1: Common failures of silicon crystalline photovoltaic modules ... 15

Figure 2.1: Working principle of a PV module ... 17
Figure 2.2: Global production process of PV modules ... 18
Figure 2.3: (a) Mono crystalline PV cell and (b) multi crystalline PV cell ... 18
Figure 2.4: Cross-section of a p-type BSF crystalline silicon PV cell ... 19
Figure 2.5: Bifacial (a) PERC cell and (b) PERT cell ... 19
Figure 2.6: Cross-section of a PV module ... 21
Figure 2.7: Inverter with a line-frequency transformer (a) and high-frequency transformer (b) ... 21
Figure 2.8: Transformer-less inverter ... 21
Figure 2.9: Two diode model ... 22
Figure 2.10: IV-curve ... 23
Figure 2.11: IV curves with different series resistance ... 23
Figure 2.12: IV curves with different shunt resistance ... 24
Figure 2.13: EL images of solar cells: (a) without defects; (b) with a crack ... 25
Figure 2.14: Schematic layout of the Fast Optical Measurement System ... 26
Figure 2.15: Cross-section of a PV cell with a stacking fault in which the Na+ ions diffuse ... 27
Figure 2.16: HAADF image of a stacking fault ... 28
Figure 2.17: Images of a stacking fault ... 28
Figure 2.18: Proposed PID-p mechanism in n-type cells ... 29
Figure 2.19: Foil method preparation ... 30
Figure 2.20: Test setup to accelerate the migration of Na^+ ions towards the photovoltaic cell ... 30
Figure 2.21: Schematic of the corona discharge setup ... 31
Figure 2.22: Schematic of the PIDcon setup ... 31
Figure 2.23: IV curve of a p-type silicon PV cell before and after PID test ... 32
Figure 2.24: IV curve of an n-type silicon PV cell before and after PID test ... 32
Figure 2.25: Light IV curve (a) and dark IV curve (b) of solar cells with different PID ... 32
Figure 2.26: Normalized module power ... 33
Figure 2.27: EL images of p-type silicon PV cell s before (left) and after (right) PID test ... 34
Figure 2.28: EL images for a n-type silicon PV cell (a) before PID test and (b) after PID test ... 34
Figure 2.29: An example EQE measurement ... 35
Figure 2.30: EQE of an n-type silicon PV cell before PID test (a) and after PID test (b) ... 35
Figure 2.31: EBIC image of a PV cell with shunts from PID ... 35
Figure 2.32: DLIT image of a PV cell with shunts from PID ... 36
Figure 2.33: Leakage current for mono-crystalline Si modules at different temperatures ... 36
Figure 2.34: Voltage divider model for PID on module level ... 38
Figure 2.35: Schematic of the thermal recovery process ... 39

Figure 3.1: LOANA solar cell analysis system ... 42
Figure 3.2: High voltage source ... 43
Figure 3.3: Keithley 2400 front interface ... 43
Figure 3.4: Binder KB 53 climate chamber ... 43

Figure 4.1: Design of the switch matrix setup ... 45
Figure 4.2: Schematic of the reed relays used to switch between the modules for measuring ... 46
Figure 4.3: Schematic of the high voltage polarity switching ... 47
Figure 4.4: Front panel of the switch matrix ... 47
Figure 4.5: Schematic of the PCB to control the reed relays ... 48
Figure 4.6: Main tab of the LabVIEW program ... 49
Figure 4.7: Settings tab of the LabVIEW program ... 49
Figure 4.8: File hierarchy of LOANA files ... 50
Figure 4.9: Generated graphs of (a) light IV, (b) dark IV, (c) EQE and (d) normalized EQE ... 51
Figure 4.10: Generated graphs of all samples of (a) %PID, (b) %FF, (c) Voc and (d) Isc ... 51
Figure 4.11: General sheet with the five necessary columns ... 52

Figure 4.12: File hierarchy of thin film files 52
Figure 4.13: File hierarchy of switch matrix files 52
Figure 4.14: Graph of R_{sh} values of each module 53
Figure 4.15: Resulting image of EL-photos 53
Figure 4.16: Processing tab of the Python program 54
Figure 4.17: Graphs tab of the Python program 54

Figure 5.1: PV-laminate 55
Figure 5.2: Comparison of the samples after stressing 56
Figure 5.3: Dark IV data every 15 minutes obtained from the switch matrix setup 57
Figure 5.4: Dark IV data every 6 hours obtained from the switch matrix setup 57
Figure 5.5: R_{sh} as a function of stress duration 58
Figure 5.6: Light IV curve 58
Figure 5.7: PID percentage as a function of stress duration 59
Figure 5.8: EL images at different stress durations 59
Figure 5.9: Normalized dark IV as a function of the normalized light IV 60
Figure 5.10: Comparison of the samples after curing 61
Figure 5.11: Dark IV data obtained from the switch matrix setup 61
Figure 5.12: R_{sh} as a function of curing duration 62
Figure 5.13: %PID as a function of the stress duration 62
Figure 5.14: Light IV curve before stressing, after stressing and after curing 63
Figure 5.15: EL images at different stress durations 63

List of abbreviations

AC	Alternating Current
Al	Aluminium
ARC	Anti-Reflective Coating
BSF	Back-Surface Field
CCD	Charge-Coupled Device
c-Si	Crystalline Silicon
DC	Direct Current
DLIT	Dark Lock-In Thermography
EBIC	Electron Beam Induced Current
EDX	Energy-Dispersive X-ray spectroscopy
EL	Electroluminescence
EQE	External Quantum Efficiency
ESE	Energy Systems Engineering
EVA	Ethylene Vinyl Acetate
FF	Fill Factor
FOMS	Fast Optical Measurement System
FTPS	Fourier Transform Photocurrent Spectroscopy
GUI	Graphical User Interface
HAADF	High-Angle Annular Dark-Field
HV	High Voltage
I_{mpp}	Maximum Power Point Current
I_{sc}	Short Circuit Current
IV	Current-Voltage
j-box	Junction-Box
K2400	Keithley 2400
LBIC	Laser Beam Induced Current
LED	Light Emitting Diode
LCOE	Levelized Cost Of Energy
Na	Sodium
PA	Polyamide

PCB	Printed Circuit Board
PERC	Passivated Emitter and Rear Cell
PERT	Passivated Emitter Rear Totally diffused
PET	Polyethylene Terephthalate
PID	Potential-Induced Degradation
PID-p	Potential-Induced Degradation of the Polarization type
PID-s	Potential-Induced Degradation of the Shunting type
PIL	Python Image Library
P_{mpp}	Power on Maximum Power Point
PO	Polyolefin
P_t	Virtual Maximum Power
PV	Photovoltaic
PVF	Polyvinyl Fluoride
R_s	Series Resistance
R_{sh}	Shunt Resistance
SiN_x	Silicon Nitrate
SMU	Source Measuring Unit
STC	Standard Test Conditions
STEM	Scanning Transmission Electron Microscopy
TEM	Transmission Electron Microscopy
UV	Ultraviolet
VI	Virtual Instrument
V_{mpp}	Maximum Power Point Voltage
V_{oc}	Open Circuit Voltage

Abstract

The Energy Systems Engineering (ESE) research group in the UHasselt engineering technology department focusses on various reliability aspects of photovoltaic (PV) systems. One of these aspects is potential-induced degradation (PID) of PV modules, which has been shown to drastically reduce PV performance in the field and thus increasing the levelized cost of energy (LCOE). Until now, intermediate characterization of the PV modules under accelerated PID tests are conducted manually, resulting in a time-consuming occupation.

This study focused on reducing the labour time during such accelerated PID tests, which is achieved by automating the two most time-consuming operations in this process: (i) intermediate PV module characterization and (ii) processing of the acquired data. The first part is accomplished by designing and implementing a switch matrix able to automatically and *in-situ* characterize the PV modules while under PID stress. The second part is realized by a self-developed software tool which automatically post-processes the data after the PID experiment.

In order to verify the correct operation of the self-developed tools, accelerated PID tests were conducted on five single-cell PV modules. Indeed, the tools are shown to operate properly by executing the PID stress test and automatically post-processing the data successfully. On top of the basic requirements set by ESE, the tool is also able to reverse PID stress *in-situ* while the characterization continues.

Samenvatting

De Energy Systems Engineering (ESE) onderzoeksgroep van de UHasselt afdeling ingenieurswetenschappen focust op verschillende betrouwbaarheidsaspecten van fotovoltaïsche (PV) systemen. Een van deze aspecten is *potential-induced degradation* (PID) van PV-modules. Hiervan is aangetoond dat het de PV-prestaties drastisch verlaagd en daarmee de *levelized cost of energy* (LCOE) verhoogt. Tot nu toe wordt de tussentijdse karakterisering van de PV-modules onder versnelde PID-tests handmatig uitgevoerd, wat resulteert in een tijdrovende bezigheid.

Deze studie richtte zich op het verminderen van de arbeidstijd tijdens dergelijke PID-testen, hetgeen bereikt werd door de twee meest tijdrovende operaties in dit proces te automatiseren: (i) tussentijdse karakterisatie van de PV-modules en (ii) verwerking van de verkregen gegevens. Het eerste deel is bereikt door het ontwerpen en implementeren van een *switch matrix* die in staat is om automatisch en *in-situ* de PV-modules te karakteriseren terwijl ze onder PID-stress staan. Het tweede deel is gerealiseerd met een zelfontwikkelde softwaretool die de data na het PID-experiment automatisch verwerkt.

Om de juiste werking van de zelfontwikkelde hulpmiddelen te verifiëren, werden versnelde PID-tests uitgevoerd op vijf eencellige PV-modules. Deze tools blijken inderdaad correct te werken door de PID-stresstest uit te voeren en de data automatisch met succes te verwerken. Bovenop de basisvereisten van ESE is de tool ook in staat om de PID-stress *in-situ* om te keren terwijl de karakterisering doorgaat.

1 Introduction

The research group Energy Systems Engineering (ESE) from Hasselt University, led by prof. dr. Michaël Daenen, is situated in EnergyVille in Genk. Since 2014, ESE has been expanding its expertise in various durability and reliability aspects of photovoltaic (PV) modules. For this purpose, ESE works closely with imec. Durability and reliability are important factors for PV modules, they determine the performance and failure rate. The more electricity a module produces over its lifetime, the better the levelized cost of energy (LCOE), which defines the cost of the module per kWh it produces during its lifetime. Thus, the more durable and reliable a module is, the more efficient the modules are, the better the LCOE. When a module performs below 80% of its initial efficiency or a safety problem occurs, the lifetime of this module is considered to be over. On Figure 1.1, common failures of silicon crystalline PV modules are shown. These failure mechanisms reduce the lifetime of a module drastically. Infant failures occur immediately in the working life of a PV module, such as contact failure in the junction-box (j-box), string interconnect, glass breakage, and loose frame. These failures are noticed immediately and are the responsibility of the manufacturer. Potential-induced degradation (PID), diode failure, and cell interconnect breakage manifest before the midlife of the module. The other failures, such as glass anti reflective coating (ARC) degradation, ethylene vinyl acetate (EVA) discolouring, delamination, cracked cell isolation, and corrosion of cell and interconnection occur later in the life of a module. To produce long-term stable PV modules, it is important to know how the long-term failure mechanisms develop [1].

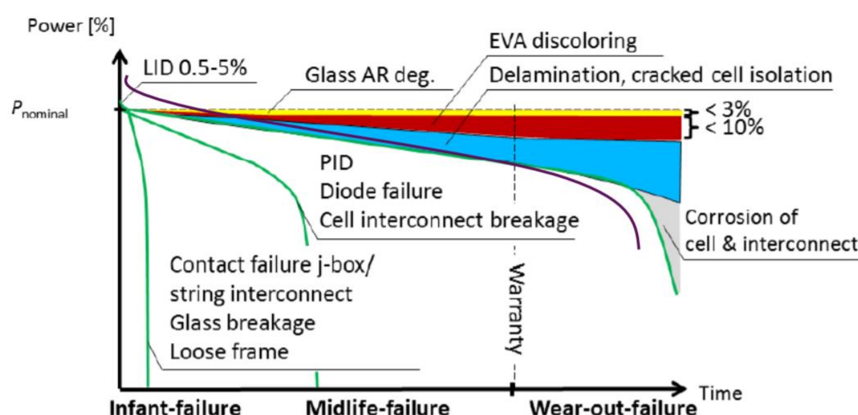

Figure 1.1: Common failures of silicon crystalline photovoltaic modules [1, p. 10]

One of the research fields of ESE is PID of PV modules. Research to prevent PID is important, as PID can reduce the efficiency of PV modules drastically before half of a module's normal lifetime. Thus, preventing PID is desired to obtain the best possible LCOE. A high potential difference between the frame and the PV cell causes PID to occur. This potential difference is created at the end of large strings of PV modules which are connected in series. The modules at the end of these strings are especially sensitive to PID as they receive the highest voltages between their cell and frame. Because of the noticeable efficiency loss PID induces on the modules, it is important to research the cause of PID, how to prevent it, and how to recover modules that suffer from PID.

To research PID, PV modules are stressed, artificially aging the cell and inducing PID. The modules need to be measured regularly to observe how the PID is developing. The measurements are done with the pv-tools LOANA. The LOANA outputs files with the measured data. The data is then manually entered in one Excel file to give a clear view of the data with the use of graphs. Moreover, electroluminescence (EL) photos are taken of the PV modules. These photos are also manually combined to form a uniform image. To be able to stress a module, an electric potential difference is

forced between the surface of the front glass and the cell. An aluminium (Al) foil is attached on top of the glass as an electrode, this creates an equal electric field over the entire glass. To measure the modules with the LOANA, the Al-foil needs to be removed. This stressing preparation and the data processing tasks are labour time consuming. Furthermore, it is possible that the PV cells are measured when the degradation has not progressed much or that the cells are not measured when a sudden increase of PID occurs.

The goal of this Master's thesis is to create a way to automate the measurements of PID. This is achieved by creating a switch matrix setup to automatically, and *in-situ*, measure the dark IV of the PV modules under stress. This way, more measurements can be performed getting a more accurate image of how PID develops. Because the module has to be covered with an electrode for stressing, only dark IV measurements are possible as no light can reach the cell. Therefore, it is still necessary to use the LOANA to measure the light IV curve and external quantum efficiency (EQE) response regularly.
A second necessity is the automation of the data processing. This covers processing the measured data and collecting it in one file. Finally, a method is required to derive the degradation percentage from the dark IV measurements and finding trends.

In Chapter 2 the literature review is discussed. This chapter contains information about solar cells and PID. Photovoltaics (Section 2.1), photovoltaic characterisation (Section 2.2) and PID of photovoltaics (Section 0) are explained. In Chapter 3, the materials and methods required to accomplish the goals are discussed. The software (Section 3.1) and hardware (Section 0) used in this thesis are explained. Chapter 0 discusses the design results. The switch matrix (Section 4.1) and the data automation (Section 4.2) are explained in detail. In Chapter 5, the PID-s test with the switch matrix is discussed. The experimental setup (Section 5.1), the results (Section 0) and the discussion and conclusion of the test (Section 5.3) are explained. Chapter 6 presents the conclusion

2 Literature review

2.1 Photovoltaics

A photovoltaic (PV) cell is a PN-junction, this means it is made out two layers of semi-conductive material. One layer is positively doped, and the other layer is negatively doped. This PN-junction is also used as the basis for a diode. Figure 2.1 shows the section of a photovoltaic cell. When light illuminates the PV cell, the photons of the light give the electrons of the semi-conductive material enough energy to break free, and an electron-hole pair is formed. The electrons will go through the metallic conducting strips on top of the cell. These strips form the negative connection. On the backside of the cell is a metal/conductive layer, this layer makes the positive connection of the cell. When the electrons are flowing, a DC voltage is created [2].

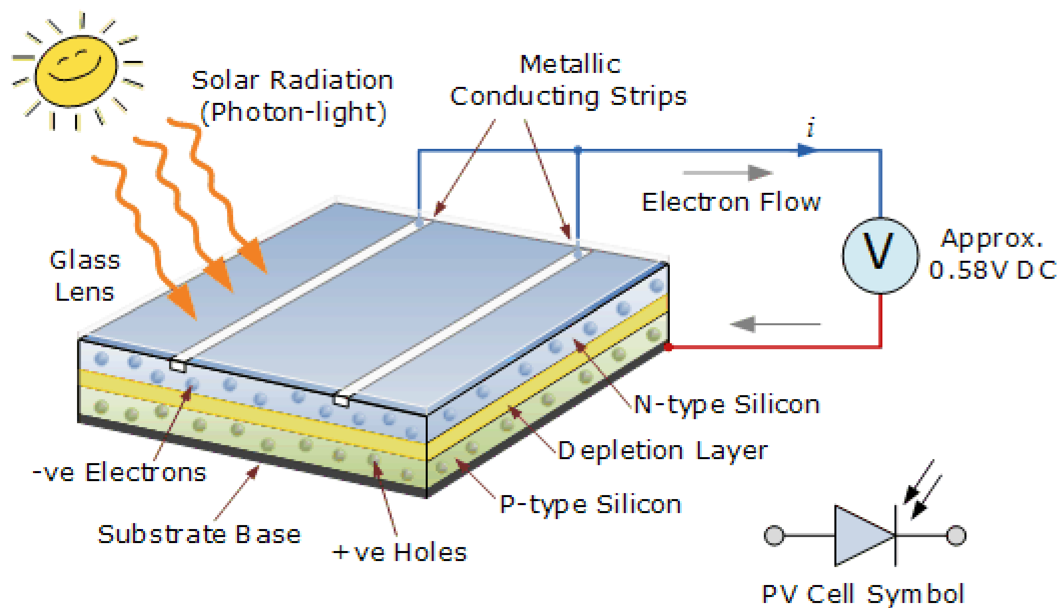

Figure 2.1: Working principle of a PV module [2]

2.1.1 Photovoltaic cells

2.1.1.1 Crystalline silicon photovoltaic cells

The development of crystalline silicon (c-Si) PV cell s was started over 60 years ago. Silicon is harmless for the environment and is one of the most common resources on earth. The subdivision of the cells is formed by the different crystalline structures.

2.1.1.1.1 Mono and multi crystalline silicon photovoltaic cells

The production process of mono and poly crystalline modules is shown on Figure 2.2. High-purity silicon goes through the Czochralski process to give all the silicon the same crystalline structure. The Czochralski method is used to grow large scale single crystals of semiconductors, metals, salts and gemstones [3]. The full method can be found in [3].

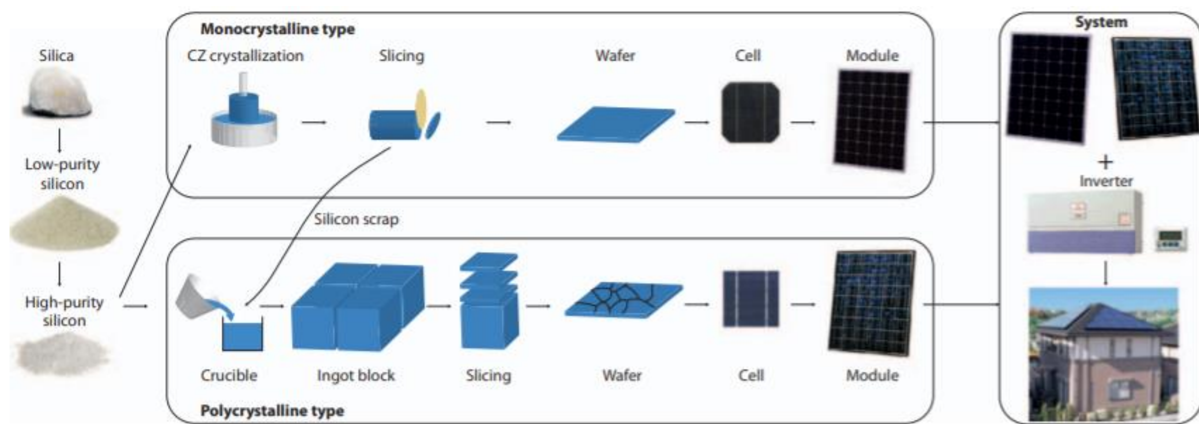

Figure 2.2: Global production process of PV modules [4, p. 97]

Mono crystalline cells (Figure 2.3a) are produced as one continuous crystal with the use of the Czochralski process. This process makes a round shaped single crystal. However, the form of the cells is square. Therefore, the edges of the round wafers are cut to make the cells square. This creates a lot of silicon that goes to waste [5]. This waste is molten and poured into a mould where it cools down. Multi crystalline cells are fabricated with this waste [3]. The process creates different grains in the silicon. These grains introduce extra defect energy levels, which creates high localized regions of recombination. By blocking carrier flows and providing shunting paths across the PN-junction for current flow, the grain boundaries reduce photovoltaic cell performance [6].

Crystalline PV cells have an efficiency between 19,8% and 18,5% for mono and multi crystalline cells with traditional aluminium back surface field (BSF), respectively [7]. The mono crystalline modules have a higher efficiency because they have one continuous crystal structure, without any grain boundaries. Multi crystalline modules have a slightly lower efficiency than the mono crystalline cells. However, they are cheaper than the mono crystalline cells due to the cheaper production process. Because the multi crystalline cells are cheaper and produce almost the same efficiency as the mono crystalline cells, they are more commonly used [5].

A disadvantage of the multi crystalline cells, is that because of the grain boundaries, they are more prone to defects. This results in a lower lifespan than the mono crystalline cells [5]. A last, important aspect is the aesthetics. The mono crystalline cells have a more uniform appearance and blend in better with darker roofs than the speckled blue colour of the multi crystalline cells [5]. The difference is clearly observable on Figure 2.3.

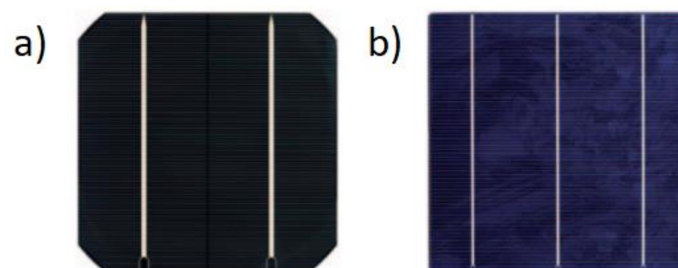

Figure 2.3: (a) Mono crystalline PV cell and (b) multi crystalline PV cell [4, p. 96]

The efficiency of the cell is increased by reducing the light reflection. This is achieved by texturing the front surface of the cell. This means that the surface is full of micrometre sized pyramid structures. These pyramids are square based, upright and of random size and are distributed randomly [4], [8]. Further reduction of the reflection loss is achieved by applying an anti-reflective coating (ARC) on top of the textured surface of the cell. This coating is made of silicon nitride (SiN_x) [4].

Another technique to increase the efficiency is to reduce the surface recombination. The reduction of surface recombination is referred to as passivation [9]. Structures with dielectric surface passivation and partial contacts suppress surface recombination. This structure is called passivated emitter and rear cell (PERC). The internal reflection of long-wavelength light is improved by a PERC cell. SiN_x is a passivation layer with a high positive charge. Another passivation layer is Al_2O_3, which has a high negative charge. These days, Al_2O_3 with an extra SiN_x capping layer is used in PERC cells. These PV cells have conversion efficiencies of approximately 21% and 22% for multi and mono crystalline silicon, respectively. With the use of a BSF, the electrical quality is improved of the back surface. The amount of minority carriers is reduced at the back surface by the BSF. Therefore, the recombination is decreased [10].

On the front and rear silicon surface, silver contacts (electrodes) are present to collect the majority carriers which are generated in the bulk and diffusion layers. At the front, the contact is comprised of several busbars connecting gridlines. At the back, the contact consists of a string of silver stripes [4]. Figure 2.4 shows the cross-section of a crystalline silicon PV cell. The thickness of the substrate is in the range of 160-240 µm [4].

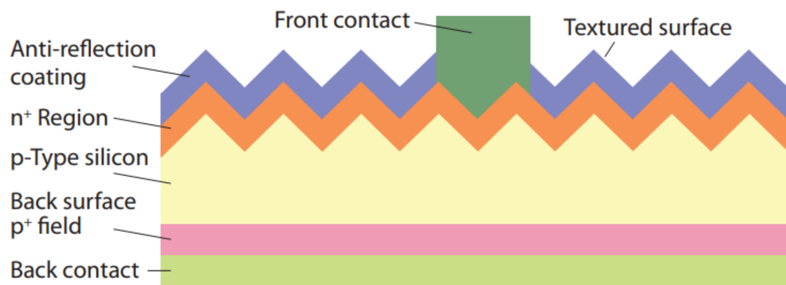

Figure 2.4: Cross-section of a p-type BSF crystalline silicon PV cell [4, p. 96]

2.1.1.1.2 Bifacial silicon photovoltaic cells

Bifacial solar cells absorb solar radiation from both the front and rear side. This way, the solar cell not only uses incident, but also albedo light. Therefore, bifacial PV modules have an increased power density compared to monofacial PV cells and the levelized cost of energy (LCOE) is reduced [11], [12]. Bifacial solar cells have an open metallization grid on both sides to enable illumination absorption from both sides [11]. Several different bifacial structures are in existence, such as passivated emitter rear totally diffused (PERT) and passivated emitter rear contact (PERC). The PERC cell, shown in Figure 2.5a, is largely constructed on p-type c-Si wafers. It has an efficiency in the range of 19,4-21,2% at the front and 16,7-18,1% at the rear side, with a bifaciality factor of approximately 80%. The bifaciality factor is the ratio of the maximal power of the rear side with respect to the maximal power of the front side. The PERT cell, shown in Figure 2.5b, is mainly founded on n-type c-Si wafers. The front efficiency is around 19,5-22% and the rear efficiency is 17-19%, resulting in a bifaciality factor of approximately 85% [13].

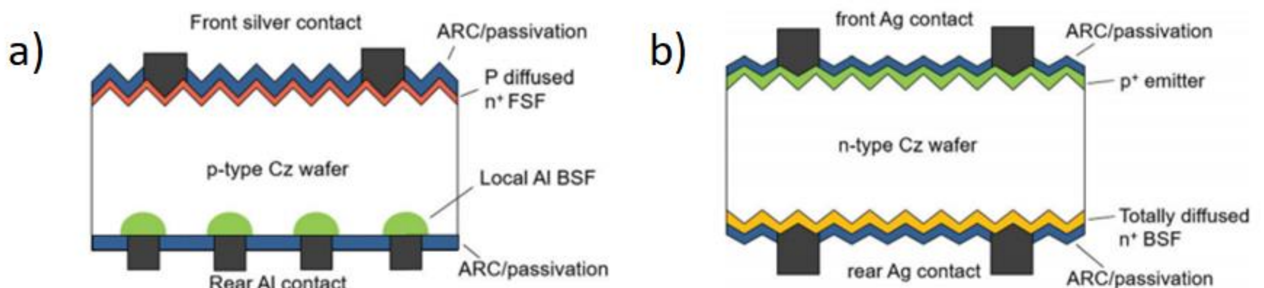

Figure 2.5: Bifacial (a) PERC cell and (b) PERT cell [13, p. 120]

The bifacial PERT cells require screen-printed finger grids on the front side, as well as the rear side of the cell. In contrast, bifacial PERC cells only use silver for the front contacts and use aluminium for the rear contacts [14]. A full area BSF is present in PERT cells, while PERC cells only have local Al BSF at the rear contacts [15].

2.1.2 Photovoltaic modules

One cell produces approximately 0,6 V. A higher voltage is necessary for the system electronics. To acquire higher voltage levels, single cells are connected in series in a PV module. A module consists of multiple sequences of cells. The front contact of one cell is connected to the back contact of the adjacent cell via soldered copper interconnects [16].

PV modules are then laminated to protect them from the environment. The packaging materials are required to withstand outdoor conditions, such as ultraviolet (UV) exposure, high temperatures, wind loading, humidity and rain. The front sheet needs to resist mechanical stress, such as high wind speeds and hail. Therefore, it is essential that it has an adequate tensile strength and is able to withstand high impact. Because it is located on top the cell, a high optical transmission is necessary. Soda-lime glass is usually used as front sheet [16].

The back sheet has the same requirements as the front sheet. However, it does not need to be optically transparent when monofacial cells are used. For bifacial cells, however, the back sheet does need to be optically transparent. Usually, a glass or a backsheet is used [11]. A back sheet usually consists of three polymeric films, with a different function, which are glued together with adhesives. The inner layer provides adhesion to the encapsulant. It is a fluoropolymer or a tie layer. The second layer ensures the electrical isolation. A polyester such as polyethylene terephthalate (PET) is traditionally used. However, thermoplastics such as polyolefin (PO) or polyamide (PA) are also possible. The outer layer requires resistance against weather conditions. Usually, fluoropolymers are used, such as polyvinyl fluoride (PVF) [16].

The encapsulant secures the cells from chemical, electrical, and physical stress. It is flexible to obstruct expansion and contraction. Furthermore, it is an electrical isolator to guarantee the functionality of the cells. Thermal conductivity is also a requirement to prevent unrestrained heating of the cells. Optical transparency is also needed. The most common encapsulant is EVA [16].
A j-box is connected. In the j-box, the interconnects of the string of cells are adapted to the connector leads of the module. It requires electrical insulation and obstruct moister intrusion to protect the internal components. Bypass diodes are integrated in the electrical circuit in the j-box. These diodes prevent damage from electrical mismatch. Electrical mismatch is due to damage, degradation of partial shading of cells. This leads to loss in power output and heat dissipation [16].
Finally, a frame is used for mechanical support and the mounting of the module. Adhesives are used between the frame and the edge of the laminate. The frame is grounded [16]. Figure 2.6 shows the cross-section of a PV module.

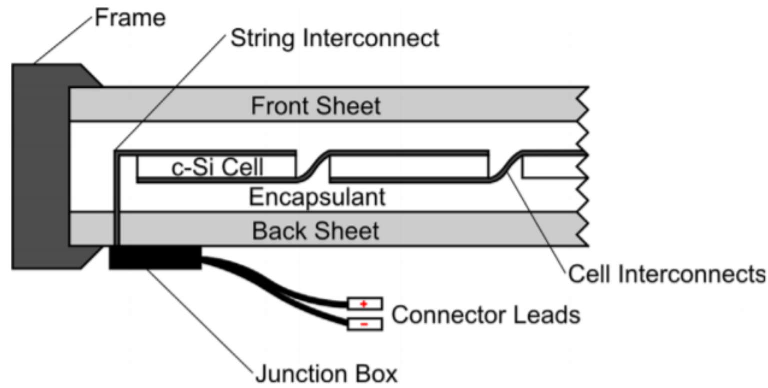

Figure 2.6: Cross-section of a PV module [16, p. 999]

2.1.3 Photovoltaic systems

PV modules produce a DC-voltage. This DC-voltage is converted to an AC-voltage by an inverter. Inverters are classified into two types: inverters with and without a transformer. Galvanic isolation is achieved between the grid and PV panel with the use of a line-frequency transformer, shown in Figure 2.7a. However, line-frequency transformers, shown in Figure 2.7b, increase the overall cost because they are large and heavy in mass. High-frequency transformers eliminate these problems. The negative or the positive pole of these inverters is grounded [17], [18].

Transformer-less inverters, shown in Figure 2.8, are smaller in size and lighter in mass, therefore, they are cost-effective. Another advantage is the increase of efficiency by 1-2%. However, no galvanic isolation is present and voltage fluctuations may occur between the ground and the PV array. Furthermore, transformer-less inverters are not required to be grounded. This causes a floating potential; thus, some cells are negatively biased while others are positively biased relative to the ground. These inverters can be grounded. However, the user is not able to choose which pole [17], [18].

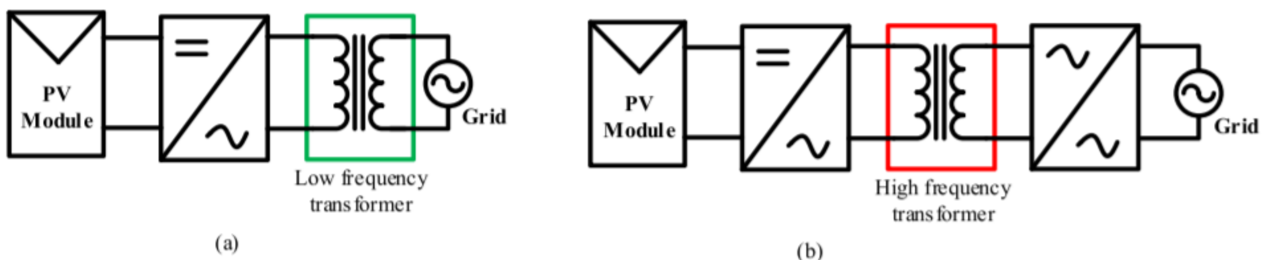

Figure 2.7: Inverter with a line-frequency transformer (a) and high-frequency transformer (b) [17, p. 1125]

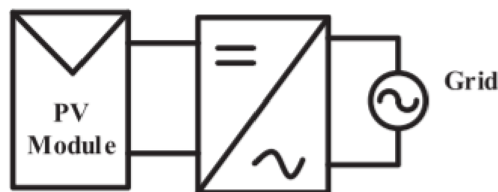

Figure 2.8: Transformer-less inverter [17, p. 1124]

2.2 Photovoltaic characterization

2.2.1 PV cell model

An ideal PV cell consists of a current source I_L in parallel with a diode. However, some corrections are made to take the losses in account. The first correction is the addition of a series resistance (R_s). This resistance corrects for the current flow resistance and electrodes resistance. Another resistance, the shunt resistance R_{sh} takes the leakage current into account. The model with the series and shunt resistance is called the single diode model. The two diode model adds another diode to correct for the recombination current loss located in the depletion region and the space-charge region. This is the most accurate model. However, the single diode model is commonly used because of its simplicity [18].

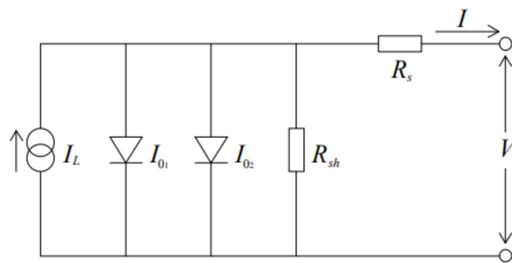

Figure 2.9: Two diode model [19, p. 565]

The two diode model has seven variables: the photocurrent I_L, the dark saturation currents of the two diodes I_{01} and I_{02}, the shunt resistance R_{sh}, the series resistance R_s, and the ideality factors of the diodes n_1 and n_2. With these parameters, the two diode model is represented by the equation (1) which describes the IV characteristic [18].

$$I = I_L - I_{01}\left(e^{\frac{V+IR_S}{n_1T}} - 1\right) - I_{02}\left(e^{\frac{V+IR_S}{n_2T}} - 1\right) - \frac{V+IR_S}{R_{sh}} \tag{1}$$

2.2.2 IV curve

2.2.2.1 Light IV

The IV-curve is a graph that displays the current as a function of the voltage. On the IV-curve, different parameters are observable. Figure 2.10 shows the open circuit voltage of the solar cell (V_{oc}), the short-circuit current (I_{sc}), and the virtual maximum power (P_t). These parameters are best case scenario and will make the solar cell the most efficient. However, a real measurement appears more like the red curve. The power at the maximum power point (P_{mpp}) of the red curve is calculated by multiplying the current at maximum power point (I_{mpp})with the voltage at the maximum power point (V_{mpp}).

With the maximum power and the virtual maximum power, the fill factor (FF) can be calculated with formula (2). This means the fill factor shows how much of the virtual reachable power is generated [20], [21].

$$FF = \frac{P_{max}}{P_t} = \frac{I_{mpp} * V_{mpp}}{I_{sc} * V_{oc}} \tag{2}$$

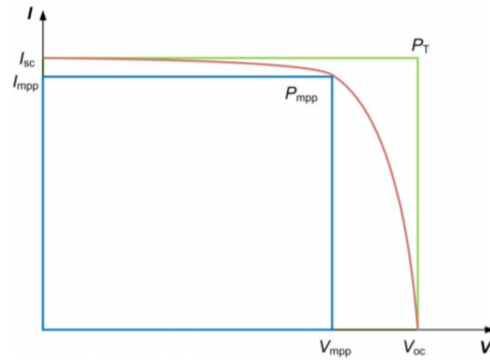

Figure 2.10: IV-curve [20, p. 27]

The maximum power is also used to calculate the efficiency η of the cell with equation (3).

$$\eta = \frac{P_{mmp}}{AI_T} \tag{3}$$

with A the solar irradiance with spectrum AM 1,5 and temperature T is 25°C [21], [22].
The series and shunt resistance of the cell has an influence on the IV-curve. When the series resistance is increased, the slope at V_{oc} is decreased. The decrease of shunt resistance increases the negative slope at I_{sc}. R_s is calculated with equation (4) [21]. The effect of the series resistance is shown in Figure 2.11.

$$R_s = -\left(\frac{dV}{dI}\right)_{V=V_{oc}} \tag{4}$$

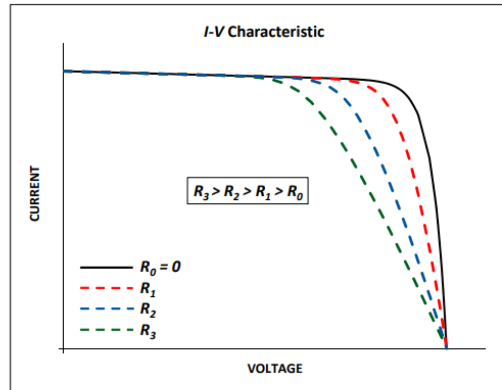

Figure 2.11: IV curves with different series resistance [19, p. 566]

Figure 2.12 shows the effect of the shunt resistance on the IV curve. The increase of the series resistance and the decrease in shunt resistance both reduce the FF, and thus the P_{mpp} [19]. R_{sh} is calculated using the slope of the IV curve at the short circuit point. Formula (5) shows this formula, this formula also corresponds to Ohm’s law [21], [23], [24].

$$R_{sh} = -\left(\frac{dV}{dI}\right)_{I=I_{sc}} \tag{5}$$

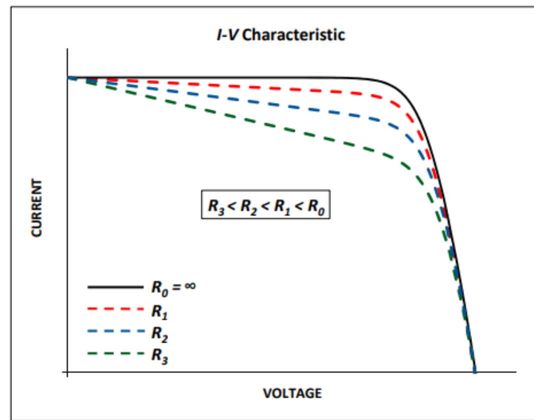

Figure 2.12: IV curves with different shunt resistance [19, p. 566]

2.2.2.2 Dark IV

In the dark, a solar cell can be specified as a simple diode. This means that in the dark the characteristic exponential diode curve can be measured [25]. To measure the dark-current, first the PV cell needs to be covered to eliminate any light to cancel out noise. Secondly, a power supply is connected to the PV cell with the same polarization as the cell. Then, the current and voltage are measured as the voltage of the power supply increases from zero to the upper limit. The dark-current flow is in the opposite direction to the light-current flow; however, the electrical configuration of the cells PN-junction is still forward biased as during typical operation [26].

2.2.3 Electroluminescence

The solar cell is a PN-junction, which works like a diode. When a DC current is sent through the solar cell, it functions as a light emitting diode (LED) [20]. Electroluminescence (EL) imaging of a solar cell under forward bias is used to investigate deficiencies and material properties [22]. Regions with high conversion efficiency have a brighter luminescence in the image, while defects such as cracks are darker. Therefore, this image highlights defects as dark objects, however, random dark spots in the background of the image provides for difficult automatic examination. These dark sports are grain boundaries and dislocations [27].

The light the Si PV cell, with a bandgap of 1,1eV, emits has an infrared radiation wavelength of around 1150nm. Therefore, it is in the infrared spectrum and not visible with the naked eye [20]. To detect the emitted light, a charge-coupled device (CCD) camera can be used in combination with a filter. The best image is taken in the dark because it cancels out the most noise [20]. To get a brighter picture (more EL light), a longer shutter time of the camera is used to capture more light. Another possibility is to put a higher current through the solar cell [28].

Figure 2.13 shows two EL images of solar cells without defects (a) and with a crack (b). The crack is noticeably darker.

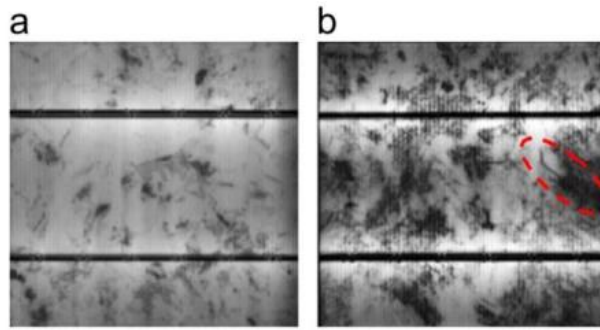

Figure 2.13: EL images of solar cells: (a) without defects; (b) with a crack [27, p. 251]

2.2.4 External quantum efficiency

External quantum efficiency (EQE) is a measuring method to get insights into the opto-electrical properties of a solar cell. The EQE measurements are used to get the spectral response of the solar cell [29]. The EQE presents the quantity of charge carriers accumulated by the cell from the quantity of incident photons at a certain wavelength. The spectral response gives insight into the output of the solar cell corresponding to a constant energy input at various wavelengths in the range of 300-1200 nm [30]. A common way to measure the EQE is by using Fourier transform photocurrent spectroscopy (FTPS). A halogen source that emits a white light is modulated by a Michelson interferometer. As a result, the different wavelengths of the white light are modulated at different frequencies. The spectral response can be gained through inverse Fourier transformation of the photocurrent when a thin film of the solar cell gets illuminated with the modulated light. This is because the photocurrent is modulated the same as the incident light [31].

Figure 2.14 shows the schematic layout of the Fast Optical Measurement System (FOMS) to measure the EQE. The light from the source is a halogen lamp because of its smooth emission spectrum. The source light (1) goes through the filter wheel (2) and a slit (3). Then the polychromatic light (4) is dispersed (5) which creates the dispersed light beam (6). The beam then illuminates the Digital Micromirror device (7) which creates two light beams (8). These two light beams are identical and directed through mixing and focussing optics (9) so that the created polychromatic light beam (10) can illuminate the device under test (11) and the reference detector (12). The final value of the measurement is obtained by dividing the demodulated photocurrent signals from the device under test (11) and the reference detector (12) on a computer (13) [31].

This is a very specific device, there are also other methods to measure the EQE, but they use the same principles. Therefore, it is unnecessary to explain all of them.

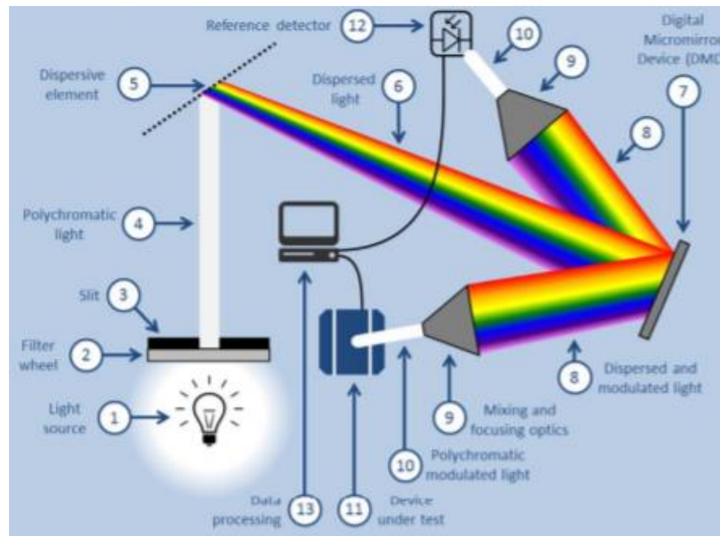

Figure 2.14: Schematic layout of the Fast Optical Measurement System [31, p. 7]

2.2.5 Electron beam induced current

Electron beam induced current (EBIC) detects doping level inhomogeneity, recombination sites and electrical irregularities in PV cell. It is very responsive to electron-hole recombination. Thus, it is useful for detecting defects which act as recombination centres. A current is put through the cell to fabricate an EBIC image. Physical defects are darker in an EBIC image than areas without physical defects [22].

2.2.6 Laser beam induced current

Laser beam induced current (LBIC) maps the photocurrent response of a PV cell. With the use of three excitation wavelengths (639 nm, 785 nm and 830 nm) provided by lasers, electron-hole pairs are created in the cell causing a DC current which is measured [22].

2.2.7 Dark lock-in thermography

Dark lock-in thermography (DLIT) imaging is used for quantitatively evaluation of inhomogeneous dark currents in PV cells. Leakage currents are indirectly detected with DLIT. A reverse bias is applied to concentrate current in shunts. A forward bias is applied to sense shunts. An infrared wavelength is transmitted by the cell and is detectable with an infrared thermal camera [22].

2.3 PID of photovoltaics

2.3.1 PID types

2.3.1.1 PID of the shunting type (PID-s)

PID-s or Potential induced degradation of the shunting type is the most common type of PID in p-type c-Si modules [32]. This degradation mode reduces the shunt resistance and increases the dark saturation current due to recombination in the space-charge region and ideality factor of the second diode term [32]. Sodium ions (Na^+) play a dominant role in the evolution of PID-s [32], [33]. An electric potential of a few volts is necessary across the SiN_x layer to induce PID-s [34]. The origin of the Na^+ ions is still unclear. Soda-lime glass contains sodium ions which accelerates PID in comparison with modules without a front glass. However, modules without a front glass still suffer from PID, thus another sodium source is present. Na contamination on the cell surface is likely another origin [35]. Then, the Na^+ ions are at the PN-junction where they create stacking faults a few micrometres through the PN-junction [36]. These small channels reduce the shunt resistance drastically. Figure 2.15 shows the cross-section of a PV cell with a stacking fault in which Na-ions diffuse under the effect of a powerful electric field. PID is especially a problem on large strings of serially connected PV modules. At the end of the string there will be a high electrical potential between the solar cell and the grounded frame driving the Na^+ in the PV cell. This leads to the shunting PID in the field [37].

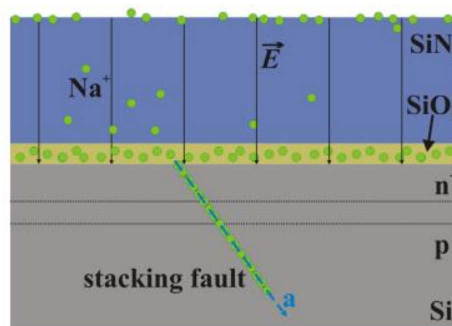

Figure 2.15: Cross-section of a PV cell with a stacking fault in which the Na+ ions diffuse [34, p. 387]

Tests indicate that the stacking faults that lead to PID-shunting do not exist until PID-stress is applied. This means that the stacking faults get decorated with Na and grow under PID at the same time. The Na atoms cause an additional stress to the dislocations and crystal faults in the Si. This stress makes the dislocations larger, leading to an in-depth growth of planar defects by splitting into partial dislocations. The stacking faults remain after the out diffusion of Na [36]. The Na decorated stacking faults are 0,57 nm wide. A shift of Si-atoms is observed as an effect of the Na within the stacking fault. Figure 2.16 shows a high-angle annular dark-field (HAADF) image of the atomic structure of the defect. The dark diagonal stripe indicates a stacking fault [34].

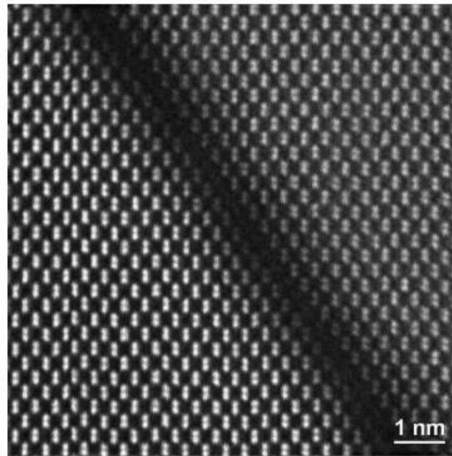

Figure 2.16: HAADF image of a stacking fault [34, p. 386]

Figure 2.17 shows a stacking fault inclined to the solar cell surface and perpendicular to the transmission electron microscopy (TEM) lamella surface. The left image gives an overview of the defect, which is nearly 2µm. The composition of the elements is obtained by energy-dispersive X-ray spectroscopy (EDX) in Scanning TEM (STEM) mode. The images on the right side show the elemental location of Na, O and N, respectively. These images show that Na is present in the stacking fault [34].

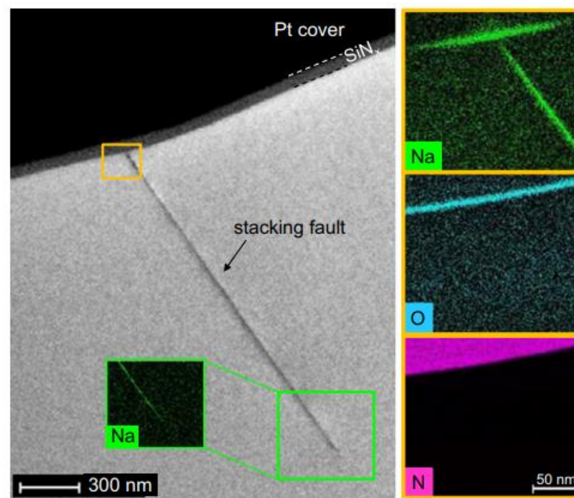

Figure 2.17: brightfield TEM image of a stacking fault (left), EDX mappings obtained in STEM mode at the stacking fault [34, p. 385]

2.3.1.2 PID of the polarization type (PID-p)

Potential-induced degradation of the polarization type (PID-p) is caused by the surface polarization on the surface of the ARC, which increases the charge recombination. PID-p reduces I_{sc} and V_{oc} [38]. By applying a high positive voltage, relative to the ground, to an n-type PV cell with an n-layer top induces PID-p. Negative charges are trapped in the ARC, which leads to a concentration increase of the minority carriers (holes) at the top of the n-layer. This increases the surface recombination. In contrast, a high negative voltage on the cell, relative to the ground, causes PID-p in a cell with a p-type layer on top. Positive chargers are trapped in the ARC, which leads to a concentration increase of the minority carriers (electrons) at the top of the p-layer. This increases the surface recombination [39]. Figure 2.18 shows the proposed PID-p mechanism for n-type PV cell s with a n-layer top (a) and p-layer top (b).

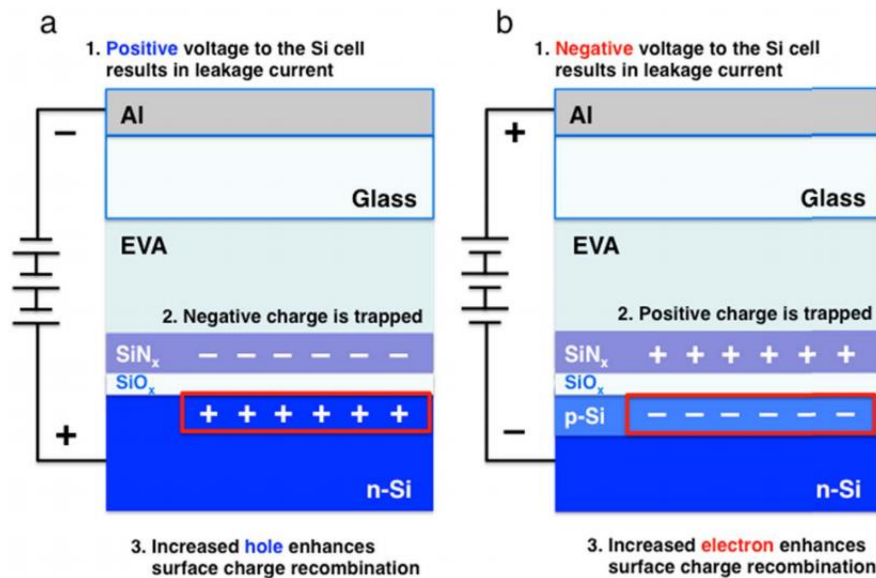

Figure 2.18: Proposed PID-p mechanism in n-type cells with an n-layer top (a) and an p-type layer top (b) [39, p. 138]

2.3.1.3 PID of the corrosion type (PID-c)

Potential-induced degradation of the corrosion type (PID-c) is caused by electrochemical reactions. Under negative bias, the grounded frame is an anode, while the metallization on the cells are a cathode. Positive charge carriers, such as Na^+-ions, migrate to the metallization. Electrons are the charge carriers in the metallization. The difference in charge carriers causes electrochemical reduction reactions. The reduction reagent is most likely water [40].

Under positive bias, oxygen and hydronium ions are generated by the oxidation of water. This results in an acidic environment close to the metal surface. Here, dissolving metals are caused through electrochemical reactions which produces acidic oxide species [40].

2.3.1.4 PID of the delamination type (PID-d)

Potential-induced degradation of the delamination type (PID-d) is caused by loss of adhesion of the laminate to the cell. The adhesion reduction is accelerated by damp heat and sodium migration. Negative voltage to the cell drives electrochemical reactions produce gaseous by-products. The gas bubbles result in metallization delamination and increased series resistance [41].

2.3.2 PID stressing methods

The PV modules that are used to test any form of PID must be stressed to generate an artificial age of 20-25 years or even more. In the process, the solar panels will be measured to see how the PID evolves [32], [33]. The test methods for PID in crystalline silicon PV modules are described in IEC 62804-1 [42].

2.3.2.1 Frame method

The moisture and temperature of the air around the solar panels have an impact on the stressing of the PV module. To emulate the outdoor conditions, a climate chamber is used. In this chamber, the temperature and humidity have to be controlled. This method stresses the cell especially around the edge, as the frame is at the sides of the cell, only stressing the outline of the cell [32], [33]. According to the IEC standard, the conditions of the frame method are: a module temperature of 60°C ± 2°C and a relative humidity of 85% ± 3% [42].

2.3.2.2 Foil method

As shown in Figure 2.19, on top of the side where normally the light falls in (only frontside on mono facial and both sides if bifacial), a metal foil, such as Al-foil or another electricity conductive material, is placed to serve as an electrode for a homogeneous distribution. The positive and negative clamp of the solar cell are interconnected. Then, a high positive voltage is put on the metal foil, the solar cell is grounded. This creates an electric field which stimulates the Na-ions to migrate towards the solar cell and cause the PID. The homogeneous electric field makes it possible to stress the cell equally everywhere. [32], [33], [28]. According to the IEC standard, the conditions of the foil method are: a module temperature of 25°C ±1°C and the relative humidity is less than 60% [42].

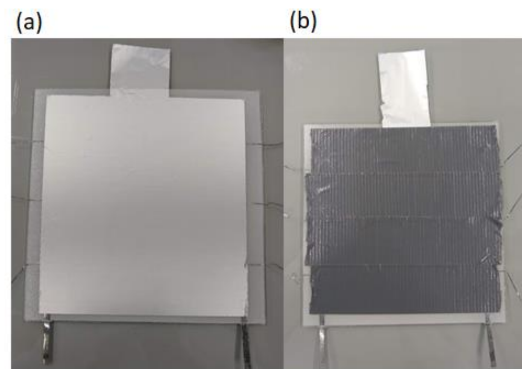

Figure 2.19: (a) shows the Al-foil on top of the PV module (b) shows the Al-foil secured with duct tape

A test setup with both the frame and the foil method is shown on Figure 2.20.

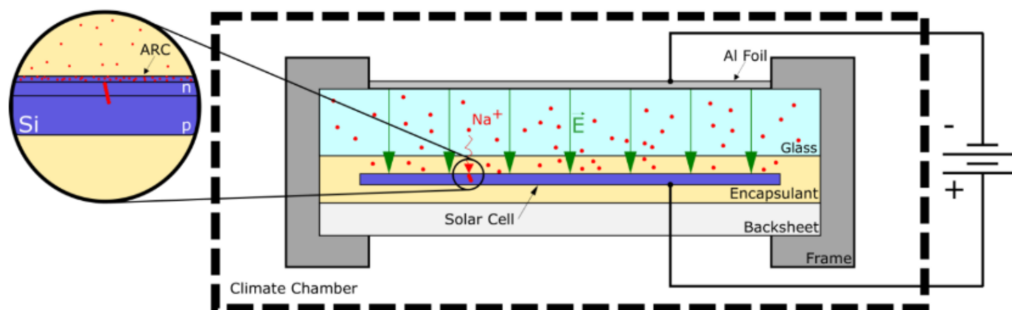

Figure 2.20: Test setup to accelerate the migration of Na^{+} ions towards the photovoltaic cell [33]

2.3.2.3 PID tests on cell level

The root cause of PID can be investigated at cell level. To do this, PID is induced in bare solar cells with a technique known as corona discharge. This is done because it is difficult to test encapsulated cells. To induce PID, a thin wire is placed in front of the front surface of the cell. By applying a high voltage on the thin wire, positive ions are located on the tip of the wire and are deposited on the front surface. Therefore, an electric field is created between the front and the back of the sample. Figure 2.21 shows a schematic of the setup. The Na, which causes PID, does not come from soda lime glass, but it is believed that it pre-exists on the surface of the cell. It is important to note that this technique ignores the influence of the glass and encapsulation material [32].

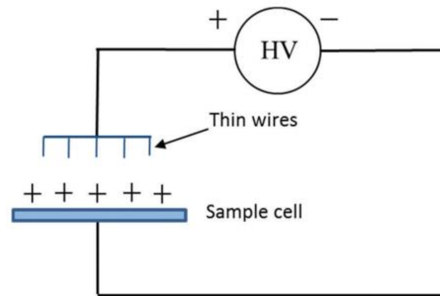

Figure 2.21: Schematic of the corona discharge setup [32, p. 53]

A PIDcon device uses a method to not only test solar cells with an ARC, but also individual components such as encapsulants and glasses. To test the cell, it requires a constant temperature. This is achieved by placing the cell on a temperature-controlled Al chuck. On top of the cell, an encapsulate layer and a glass sheet are placed. Electrical contact to the cell is realized with a needle on the front surface and the Al chunk on the rear. Figure 2.22 shows a schematic of the setup. To achieve a constant high voltage on the glass surface, a solid metal block is positioned on top of the glass. Then, a positive voltage of up to 1000 V is applied to the metal block while the Al chuck is grounded. The IV curve is measured during the test to investigate the PID process. With this method it is possible to perform tests on samples with and without laminating the encapsulant to the cell [43].

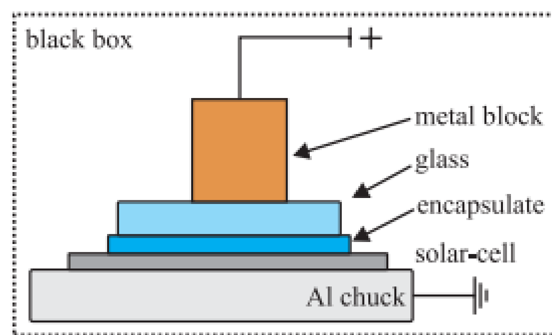

Figure 2.22: Schematic of the PIDcon setup [43, p. 835]

2.3.3 PID quantification

A few methods are used to determine the PID level of a PV module. The IEC 60904 series explains the measurement methods of PV devices [44]. The cells are tested under standard test conditions (STC), according to the IEC 60904-1 standard. These conditions are as follows: the irradiance is 1000 W/m², the cell temperature is 25°C, the spectral distribution is AM 1,5 and there is a normal incidence [45].

2.3.3.1 IV-curve

2.3.3.1.1 Light IV measurement

PID-s reduces the shunt resistance of the PV cell. The reduction of this resistance is observed in the IV curve. Figure 2.23 shows the IV curve of a p-type silicon solar cell before and after PID testing. The slope at the short circuit current decreases when the PID-s increases [38]. This causes the FF to decrease. The I_{sc} and V_{oc} are not notably affected by PID-s levels of below 40%. Once the PID-s level rises above 40%, I_{sc} and V_{oc} decrease significantly [46].

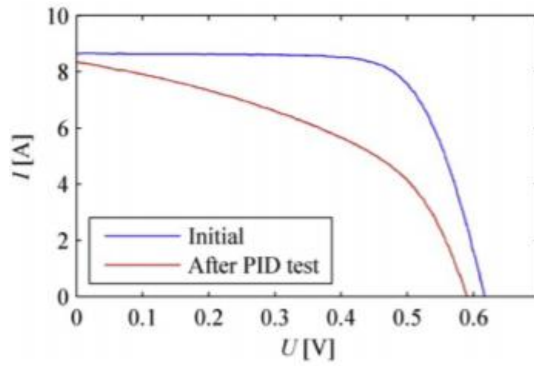

Figure 2.23: IV curve of a p-type silicon PV cell before and after PID test [38, p. 269]

PID-p is observable in the IV curve of the cell. Figure 2.24 shows the IV curve of a standard n-type silicon PV cell before and after PID testing. It is observed that the I_{sc} and V_{oc} are decreased, while the reduction of FF is insignificant [47].

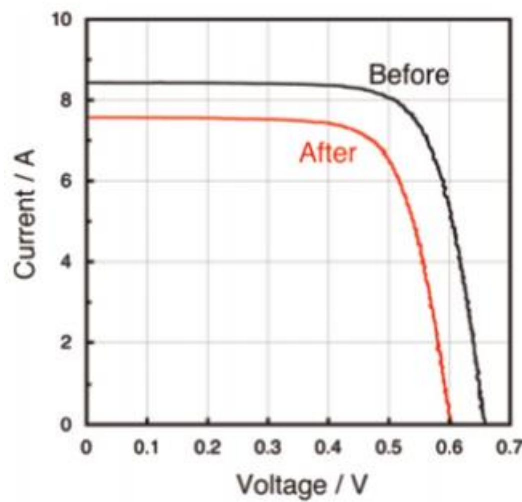

Figure 2.24: IV curve of an n-type silicon PV cell before and after PID test [47, p. 364]

2.3.3.1.2 Dark IV measurement

PID is observable in the dark IV curves as well. Figure 2.25b shows the dark IV curves of solar cells with different PID-s levels. PID(0) has the lowest PID-s and PID(4) has the highest level of PID-s. Figure 2.25a displays the light IV curve of the same solar cells. Dark IV measurements determine parameters such as series resistance, shunt resistance, diode factor and diode saturation currents.

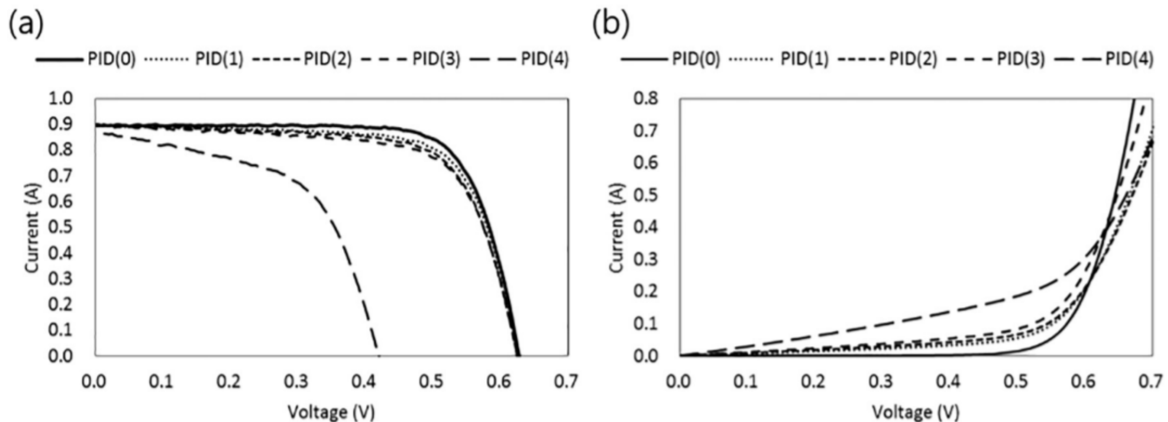

Figure 2.25: Light IV curve (a) and dark IV curve (b) of solar cells with different PID [48, p. 1000]

It is possible to estimate the module power decrease at STC from PID-s with the use of the dark IV measurement at 25°C. The dark IV derived power is necessary for this method. The dark IV derived power is calculated by shifting the dark IV curve by the average of the short circuit current before and after PID testing, following to the superposition concept. The short circuit current is acquired from the light IV measurement at STC. Figure 2.26 shows the correlation between the normalized module power of the dark IV measurement at 25°C as a function of the normalized module power of the light IV measurements under STC. The normalized power is calculated by dividing the power after testing with the power before testing. The dashed line corresponds to y = x [49].

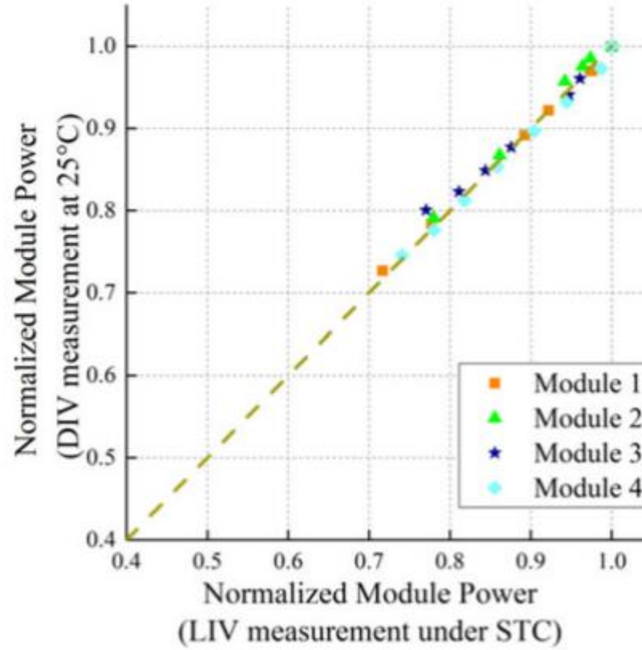

Figure 2.26: Normalized module power measured with dark IV at STC as a function of the normalized module power measured with light IV under STC [49, p. 2157]

However, PID is usually tested at temperatures higher than 25°C, to accelerate the degradation. This difference in temperature presents an error to the module power prediction by *in situ* dark IV measurements. Therefore, equation (6) is created to convert the module power derived from the dark IV at higher temperatures to the dark IV module power at 25°C [49].

$$P_{dark}(25°C,t) = \frac{P_{dark}(T_S,t)}{1+\left(1-k_{estimated}\left(1-\frac{P_{dark}(T_S,t)}{P_{dark}(T_S,0)}\right)\right)*\gamma_{dark}(0)*(T_S-25)} \tag{6}$$

$P_{dark}(25°C,t)$ and $P_{dark}(T_s,t)$ is the dark module power at stress time t, at 25°C and stress temperature respectively. $P_{dark}(T_s,0)$ is the dark module power before stressing, at stress temperature. $k_{estimated}$ is calculated with equation (7) [49].

$$k_{estimated} = \left(1-\frac{\gamma_{dark}(t_n)}{\gamma_{dark}(0)}\right) / \left(1-\frac{P_{dark}(T_S,t_n)}{P_{dark}(T_S,0)}\right) \tag{7}$$

The dark IV derived temperature coefficient γ_{dark} is calculated with equation (8). Here, $\gamma_{dark}(t_n)$ is the temperature coefficient measured at stress time t_n and $\gamma_{dark}(0)$ is measured before stressing [49].

$$\frac{P_{dark}(T_c)}{P_{dark}(T_{ref})} = 1+\gamma_{dark}(t)(T_c-T_{ref}) \tag{8}$$

$P_{dark}(T_c)$ and $P_{dark}(T_{ref})$ is the dark module power at cell temperature and reference temperature respectively [49].

2.3.3.2 Electroluminescence imaging

The EL imaging gives a general idea how the PV modules react to the PID stress [28]. PID-s is observable in EL images. Figure 2.27 shows the EL images of a standard p-type silicon PV cell before and after PID testing. The entire cell is darker after the PID test. However, some areas are degraded more than others. PID-s is caused by sodium ions migrating into the cell, which is not uniform on the surface [38].

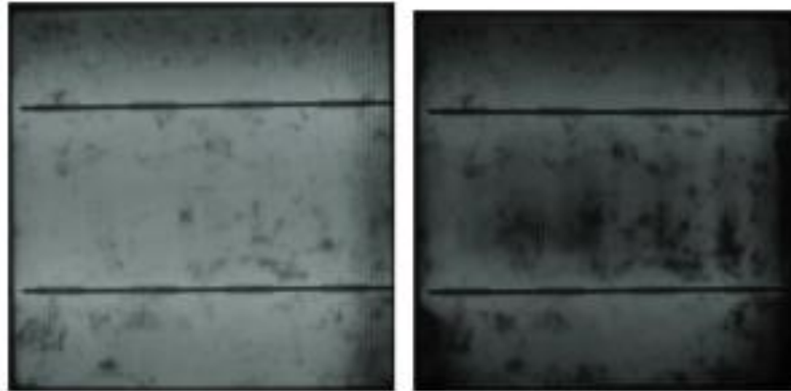

Figure 2.27: EL images of p-type silicon PV cell s before (left) and after (right) PID test [38, p. 271]

PID-p is also observable in EL images. Figure 2.28 shows the EL images of a standard n-type silicon PV cell before and after PID testing. It is observed that the entire cell is homogeneously darker after PID testing. The overall darkening is due to the polarization of PID-p, which occurs everywhere on the surface [47].

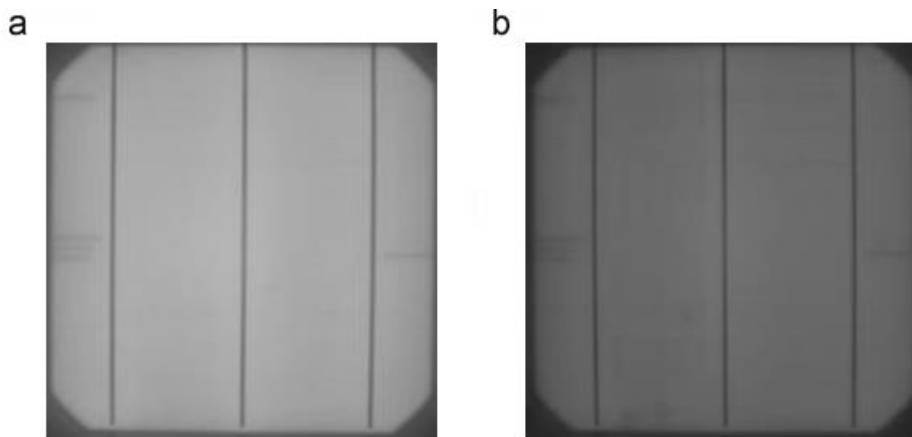

Figure 2.28: EL images for a n-type silicon PV cell (a) before PID test and (b) after PID test [47, p. 363]

2.3.3.3 External quantum efficiency

For crystalline silicon, EQE is also often used to determine the quality of the emitter and the passivation scheme [50]. Figure 2.29 shows the EQE as a function of the wavelength. The graph shows how efficient the photovoltaic cell is at each wavelength. At the lower frequencies, the efficiency of the light is reduced due to front surface recombination. In the middle range, the EQE is still not 1 (this is the maximum it can be) due to overall losses caused by reflection and a low diffusion length. At the larger wavelengths, the efficiency will go down again because the reduced absorption at long wavelengths, low diffusion lengths and surface recombination. Finally, the efficiency will go to zero once the wavelength passes the bandgap [51].

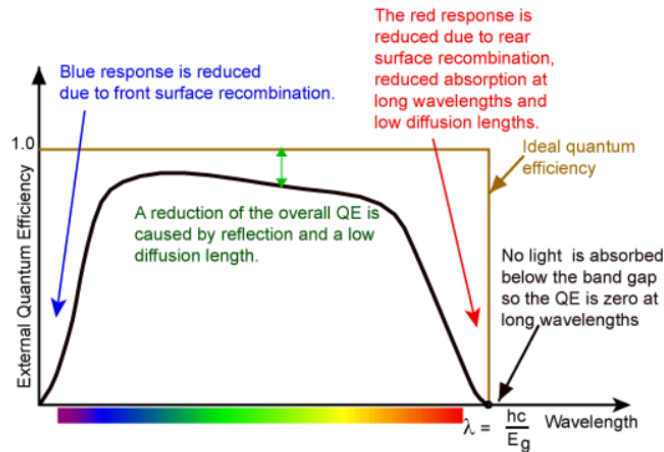

Figure 2.29: An example EQE measurement [51]

Figure 2.30 shows the EQE of a standard n-type silicon PV cell before and after PID test. The EQE is only notably decreased in the short-wavelength region from 400 to 600 nm. The increased surface recombination in the front is considered as the cause of the change in EQE. In contrast, PID-s is not observable with EQE measurements until I_{sc} starts decreasing at PID-s levels above 40% [39], [47], [52].

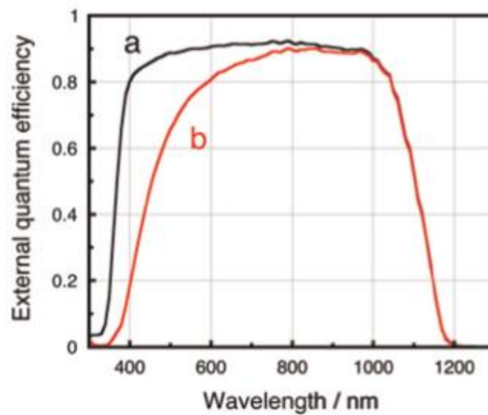

Figure 2.30: EQE of an n-type silicon PV cell before PID test (a) and after PID test (b) [47, p. 363]

2.3.3.4 Electron beam induced current

On EBIC images, particles, shunts and recombination active regions are darker, thus, PID-s is detectable. Figure 2.31 shows an EBIC image of a solar cell with PID-s. A shunt is visible as a dark region.

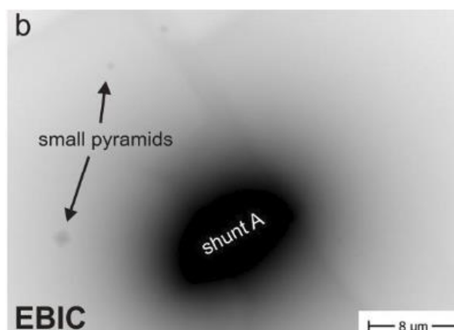

Figure 2.31: EBIC image of a PV cell with shunts from PID [53, p. 79]

2.3.3.5 Dark lock-in thermography

DLIT images are used to investigate shunts on the cell surface, thus, it is able to detect PID-s. Figure 2.32 shows a DLIT image of a solar cell with PID-s. Local shunts are observed [53].

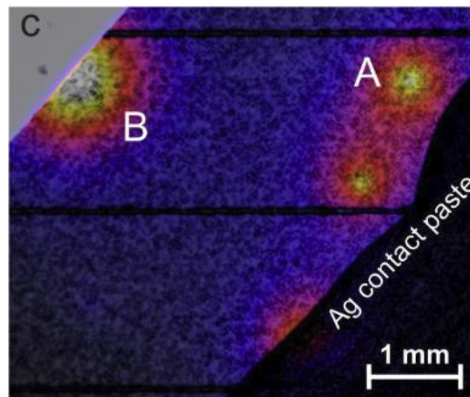

Figure 2.32: DLIT image of a PV cell with shunts from PID [53, p. 78]

2.3.4 PID kinetics

PID can behave differently under different circumstances. The main factor that changes the behaviour is the leakage current. The leakage current between the frame and the photovoltaic cell is related to PID. Reducing the leakage current by increasing the resistance between cell and frame, will slow the PID down [54]. This leakage current changes under different circumstances, mainly under temperature, humidity and the voltage between the frame and the solar cell. To be able to test PV modules, it is necessary to know how these parameters influence the PID.

2.3.4.1 Temperature

PID is caused by the migrating Na^+, the process is influenced by the temperature. The higher the temperature, the more energy the Na^+ will have, and thus more degradation because the sodium ions migrate faster. The relation between the leakage current and the temperature is an Arrhenius-type relation. Figure 2.33 shows the relation between the leakage current and the module temperature with the leakage current plotted logarithmic. This relation is exponential if the voltage and the humidity are kept constant increase [32].

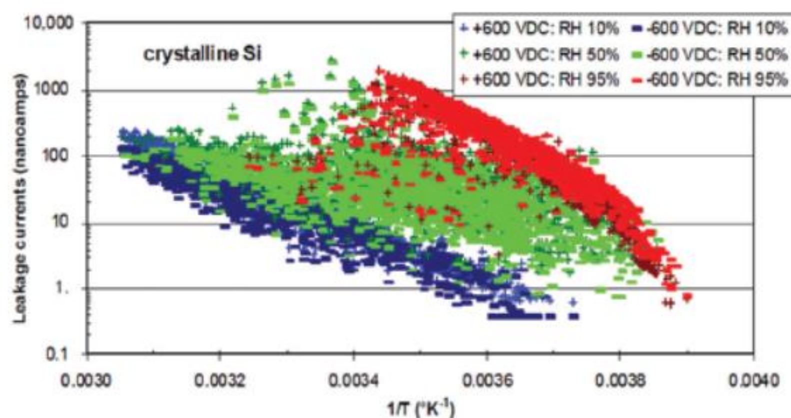

Figure 2.33: Leakage current for mono-crystalline Si modules at different temperatures and three different RH-levels [32, p. 54]

2.3.4.2 Humidity

The humidity of the climate can affect the growth of PID in multiple ways. A first effect is that at the same temperature, when the humidity is higher, the leakage current is higher [32], [55]. This can also be observed on Figure 2.33. The second effect is that the humidity affects the dominant leakage current paths. In low humidity conditions, the front glass's surface conductivity is lower than in higher humidity conditions. In this case, the surface and bulk glass conductivities dominate the leakage current. In high humidity conditions, a film is formed on the front glass which is generally not the case in low humidity. This film has a relatively high electrical conductivity. Therefore, the ionic current on the front glass becomes the predominant factor of determining the leakage currents path [32].

Finally, in the long term the humidity also influences the PID. After long periods of exposure, the moisture can penetrate the module. This increases the PID progression as the bulk resistivity of the encapsulant materials is reduced [32].

It can be concluded that the PID risk is higher when the humidity increases. In dry climates PID has shown to occur at the module edges because only the grounded frame has a high potential relative to the cell, thus sodium ions only migrate beneath the frame [32].

2.3.4.3 Voltage

The voltage between the frame and the cell is the factor for PID. With a different polarity or magnitude, the behaviour of the PID changes. The level of PID can grow in standard p-type c-Si modules if the voltage between the frame and the cell is negatively biased. The Na^+-ions are attracted towards the cell and repelled from the frame because the cell is negatively biased and the frame positively. The Na^+-ions will then migrate towards the cell as discussed in 0. With the polarity changed and thus the cell positively biased and the frame negatively, the Na^+-ions will be attracted to the frame and therefore migrate towards the frame. This can help to cure the PID or prevent it [32].

The magnitude of the voltage also has an influence on the PID behaviour. The higher the voltage, the more the PID increases [32].

2.3.5 PID preventive measures

Considering the drastic effects of PID on PV modules, methods are developed to minimize the effects. PID can be prevented at different levels: cell level, module level and system level [32].

2.3.5.1 Cell level

For p-type c-Si solar cells, the ARC has an influence on the PID susceptibility. When the refractive index increases, the PID-s resistance increases as well. This is realized by enlarging the Si/N ratio. This also ensures that the conductivity increases, and the transport of positive charges reduces onto the ARC. By reduction of the electric field and neutralizing advancing Na^+ ions, the resistance against PID is increased. A refractive index of 2.2 eliminates PID, however, the efficiency is lower due to more light absorption in the coating [32].

2.3.5.2 Module level

On module level, the leakage current can be reduced by changing the resistance of the layers between the cell and the frame. By changing the resistance of one of these layers, the leakage current can be reduced significantly, slowing down the PID [56].

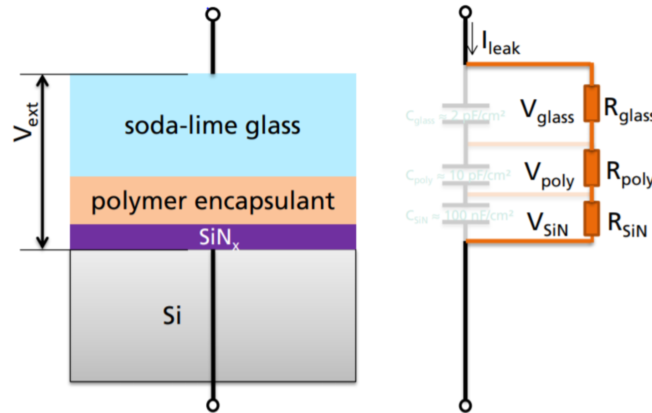

Figure 2.34: Voltage divider model for PID on module level [56, p. 10].

2.3.5.2.1 Glass

As discussed before, Na^+ causes the PID-s. The origin of the Na^+ ions is still unclear. However, PID is accelerated when soda-lime silicate glass, which contains sodium ions, is used [35]. This glass is used due to its low cost in conventional c-Si p-type modules [32]. Modules with glass without Na^+ ions are less effected by PID. An example of a glass that can be used is chemically strengthened aluminosilicate glass. Modules with conventional and aluminosilicate glass are both tested under the same conditions by [47]. These modules were stressed under -1000 V, 60°C and 85%RH with the glass surface kept wet. The power of the aluminosilicate glass modules degraded by less than 5% after 100 hours. The soda-lime glass module on the other hand lost almost 80% of their power within the first 50 hours [32], [47]. Other sorts of glass that are also reported to be able to prevent PID-s are Borosilicate- and quartz glass. The downside of these different PID-resistant glass sorts is that they all are more expensive to fabricate, which means the initial cost of the module is higher [32].

It is also possible to keep the soda-lime glass but apply a coating on the glass to stop the Na^+ migration. This layer adds an extra resistance for the leakage current. A layer that gives a significant protection against the migrating Na^+ ions under high voltage is TiO. The downside of these layers is that the optical performance of the modules decreases significantly. The extra layer reflects, absorbs and scatters the light. This leads to less light reaching the photovoltaic cell itself and thus a decrease in efficiency [32].

2.3.5.2.2 Encapsulant material

The solar cells in standard c-Si PV modules are encapsulated with an encapsulation material. This provides electrical protection for module components, a resistance to moisture, better thermal and UV degradation stability. The most commonly used encapsulant is EVA. The most important physical property of the encapsulant to PID effects is the bulk resistivity. Higher bulk resistivity leads to a smaller leakage current for a same electric potential difference, reducing voltage build-up on the solar cell surface to the solar cells and thereby mitigating PID effects [32].

2.3.5.3 System level

On system level, long serial strings of PV modules produce a DC-voltage. This DC-voltage needs to be converted to an AC-voltage. To do this an inverter is used. These inverters exist with and without a transformer [32].

The inverters that use a transformer, the negative or the positive pole needs to be grounded. As discussed before in 2.3.1.1, p-type c-Si PV modules that are negatively biased are sensitive for PID-s and PID-p. This can be taken care of by connecting the negative system pole to the ground instead of the positive pole. This causes a positively biased field and cancels out any PID-s in p-type c-Si PV modules [32]. Transformer-less inverters are floating or grounded, however, the grounded pole cannot be changed. Therefore, the solution mentioned for the inverter with a transformer cannot be used [32].

2.3.6 PID recovery

PV modules suffer from power loss due to PID, reducing the efficiency. However, research has found that most PID is reversible. PID-c and PID-s levels that is too high, cannot be recovered [32], [37].

2.3.6.1 Thermal recovery

The recovery rate of PID increases with the temperature. This is caused by the concentration difference between the Na decorated stacking fault and the oxide layer. Therefore, Na atoms diffuse out of the cells' stacking faults. The Na is relatively mobile in the oxide layer and spreads across the cell surface. In the oxide layer, this leads to a continuous low Na concentration close to the defect. Then, Na diffuses back into the ARC, however, this process is slower. Increased temperature accelerates the movement of the sodium atoms, thus accelerates the recovery [57]. Figure 2.35 shows a schematic of the thermal recovery process.

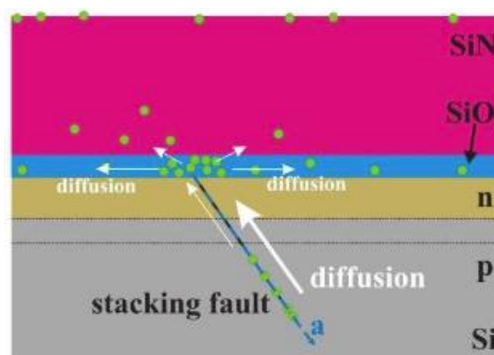

Figure 2.35: Schematic of the thermal recovery process [57, p. 492]

After recovery, the traces of PID-s were investigated by STEM. The defect is not decorated with Na after recovery. Thus, Na has diffused out of the defect. The conductive path is not conductive after recovery [37].

2.3.6.2 Voltage recovery

As discussed in 0, a high voltage between the frame and the photovoltaic cell causes PID. If the polarity of the voltage is changed and the photovoltaic cell is positively biased instead of negatively, the Na is repelled from the cell. Therefore, they migrate to the frame which is negatively biased [32].

To regenerate the PV-efficiency and have an accelerated recovery of the efficiency lost during the day, a reverse biased voltage can be applied at the modules during the night. At systems with an inverter with transformer, this method also can be used for regenerating the efficiency [32].

2.3.6.3 Light recovery

Light illumination is found to slow, or even recover, PID-p. Mainly, UV light from 300 to 400 nm is accountable for the recovery. Visible wavelengths in the range of 400 to 600 nm also recover the solar cell, however, in a lower degree. Different types of cells have different illumination recovery rates. The front side of an n-PERT cell exhibits no decrease in PID-p susceptibility under light irradiance up to 800 W/m^2. In contrast, in the rear side of an p-PERC cell, PID-p was stopped under illumination as little as 10 W/m^2. Moreover, in these cells, a full recovery in 20 minutes was observed under light irradiance of 40 W/m^2. In this case, the recovery rate surpasses the degradation, which leads to the regeneration of power. The cause of the difference in recovery rate are still unknown [58].

3 Material and methods

3.1 Software

In this Master's thesis, software is used to control the switch matrix setup and do the post process data processing. To control the switch matrix setup, LabVIEW is used. The post processing is achieved with the use of Python.

3.1.1 LabVIEW

LabVIEW, developed by National Instruments, is used to create a graphical user interface (GUI) to control the switch matrix. It is a visual programming language for system-design and development. The dataflow programming language used is called "G". Subroutines are called virtual instruments (VIs). The LabVIEW VI is composed of two features: the front panel and block diagram. The front panel is the graphical user interface. Through controls, the user can insert input to the program, and receive output from the program. The block diagram is the name of the visual source code. This code consists of controls, functions and indicators. Controls are shown in the front panel. This way, the user can specify certain parameters. Functions perform operations on its inputs to obtain an output. Finally, indicators are also shown in the front panel. It displays output to the user [59].

3.1.2 Python

Python is a high-level, interpreted, object-oriented programming language developed by the Python Software Foundation. It was used to automatically process the data from the LOANA, PME and the switch matrix measurements of the Keithley 2400 (K2400). Python has a simple syntax which strengthens the readability. Classes, modules, dynamic typing and modules are included. Python runs on Windows, Mac, and many Unix variants. The extensive standard library covers a wide range of areas such as text processing, file and directory access, file formats, generic operating system services and more. On top of this, a variety of third-party extensions is obtainable [60].

3.2 Hardware

To be able to do the measurements and stressing, extra hardware is necessary. This hardware includes everything that is required for the switch matrix setup, as well as the measuring devices used.

3.2.1 PV-tools LOANA

The pv-tools LOANA solar cell analysis system, shown in Figure 3.1, was used to do the characterisation of the PV modules. This device was utilized to do light and dark IV measurements of the modules, as well as EQE measurements. The IV measurements are realized by illuminating the module with an array of infrared LEDs to determine V_{oc}, FF, and the efficiency at arbitrary light intensities. The series resistance can also be determined with the I_{sc} and V_{oc} characteristics. To determine the short circuit current only, during the decay of a short illumination with a xenon flash while the module is in short circuit, the short circuit current is measured [61].

The EQE characteristic is measured with a focussed light spot of 20 x 20 mm from the monochromator. The monochromator can project light between 280-1600 nm with a wavelength accuracy of 1nm. In our measurements, the monochromator is used between from 280 nm to 1200 nm with a step of 10 nm [61], [62].

Figure 3.1: LOANA solar cell analysis system [61]

3.2.2 EL-camera

EL-photos of the PV modules are acquired with a Nikon D5500 camera. The single-lens reflex CMOS camera takes digital photos with an image size of 6000x4000 pixels [63]. To make the camera suitable to take EL-photos, the IR-filter of the camera was replaced with a visible light filter.

3.2.3 High voltage source

The high voltage source (HV-source), shown in Figure 3.2, was custom-made for the ESE research group. It is used to stress the PV modules for PID. The device is capable of generating voltages ranging from -2000 V to +2000 V. The maximum current it can deliver is 5 mA. The source can be controlled via a computer or used as a standalone source. In the switch matrix setup, it will be controlled via LabVIEW.

Figure 3.2: High voltage source

3.2.4 Keithley 2400

The Keithley 2400, shown in Figure 3.3, is a source measure unit (SMU). It can do a voltage sweep and measure the current, this makes an IV curve. The Keithley 2400 can handle a maximum of 1 A at 20 V and 0,1 A at 200 V, for a maximum power draw of 20 W. It is possible to use the Keithley 2400 via LabVIEW. LabVIEW is used to provide the Keithley 2400 with the right parameters and can also collect the measured data. The connection between LabVIEW and the Keithley 2400 is done with GPIB, it can handle up to 1700 reading/second at 4,5 digits via GPIB [64].

The measurement performed is a 4-wire measurement. With the four wires, it is possible to source the voltage while measuring the current. This cancels out any interference of the wires and reed relays to get a more accurate measurement. To make an IV curve, the voltage is sourced using a linear staircase sweep. This sweep changes the voltage from the start level to the stop level in linear steps [64].

Figure 3.3: Keithley 2400 front interface [65]

3.2.5 Climate chamber

The Binder model KB 53 climate chamber, shown in Figure 3.4, was used to control the test environment. This device is able to reach temperatures up to 100°C. Furthermore, it has two stainless steel racks to place the PV modules on [66].

Figure 3.4: Binder KB 53 climate chamber [66]

4 Design results

4.1 Switch matrix

To automate the dark IV measurements and PID stressing, a switch matrix is necessary. The switch matrix can switch the high voltage mechanically on or off. It can also invert the polarity of the HV-source, making it possible to stress and cure the modules. By connecting the modules one by one to the K2400, it is possible to measure the modules *in-situ*. This data is sent directly to the laptop controlling the switch matrix setup.

4.1.1 Setup

The design of the setup, in which the switch matrix is use, is shown in Figure 4.1. A laptop, running the custom LabVIEW program, is connected to the K2400, a HV-source, and the switch matrix. The high voltage outputs of the HV-source are connected to the switch matrix. In the switch matrix, the high voltage can be switched on and of mechanically with the use of reed relays. The high voltage should never reach the K2400, as it is not designed to withstand such high voltage. Therefore, before measuring, the HV-source is shut of through LabVIEW and the reed relays of the high voltage input are switched open to make sure no voltage will be over the K2400 terminals. The high voltage polarity can also be inverted with the switch matrix, switching the plus and minus, while the ground connection will always stay the same. The K2400 is used to measure the dark IV curves. Reed relays are used to switch between stressing and measuring the modules. These reed relays are controlled by an Arduino Nano via LabVIEW. The Arduino and all the reed relays are located in the switch matrix. Figure 4.1 shows two PV modules connected to the switch matrix, however, up to six modules can be connected.

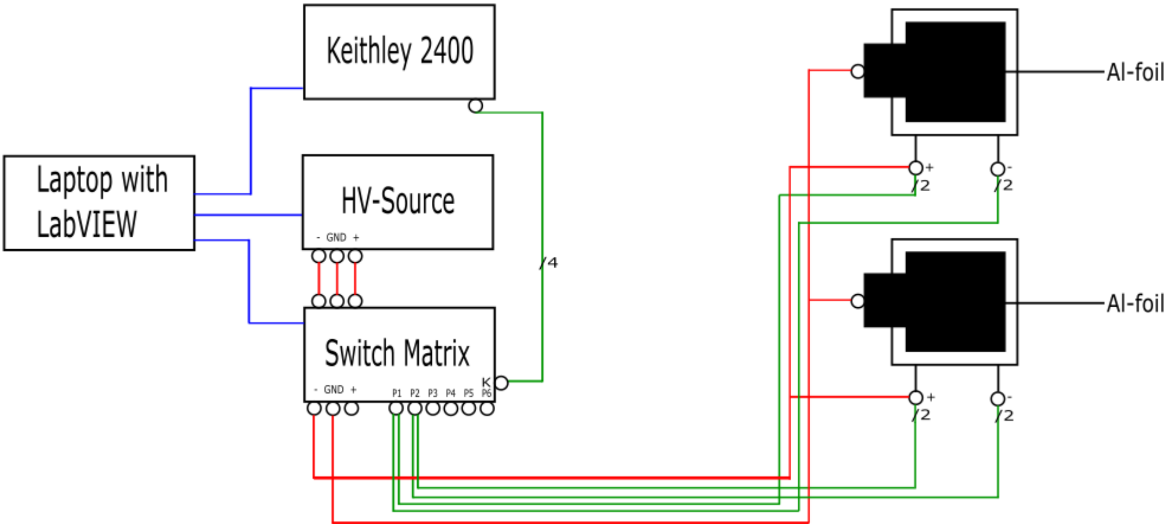

Figure 4.1: Design of the switch matrix setup. The blue lines are USB cables, the red lines are high voltage cables, and the green lines stand for 2 wires to connect the modules. In this case, two PV modules are connected, maximum six modules can be connected

4.1.2 Photovoltaic characterisation

The schematic used for switching the modules for measuring is shown in Figure 4.2. The schematic is portrayed for two modules. The switch matrix is accommodated for maximum six modules.
The left reed relays in Figure 4.2 are used to short the positive and negative output of the module. This is done when the module is stressed (or cured) and is therefore activated at the same time as the HV-source. When the cell is measured, these reed relays interrupt the circuit.

The other four reed relays are activated when the specific module requires to be measured. For example, when module one needs to be measured, only the four reed relays of module one are activated. These are deactivated as soon as the measurement is finished.

Because of the high voltage present in the switch matrix, a good isolation is necessary to ensure there are no voltage sinks. Therefore, reed relays are used. The used reed relays can switch up to 10 kV and a maximum current of 3 A. They are not only used for switching the high voltage but also for the separation between the modules and the K2400 because of their breakdown voltage of 15 kV [67]. They are chosen for their low contact resistance (150 mΩ [67]), quick switching, and simple control circuit.

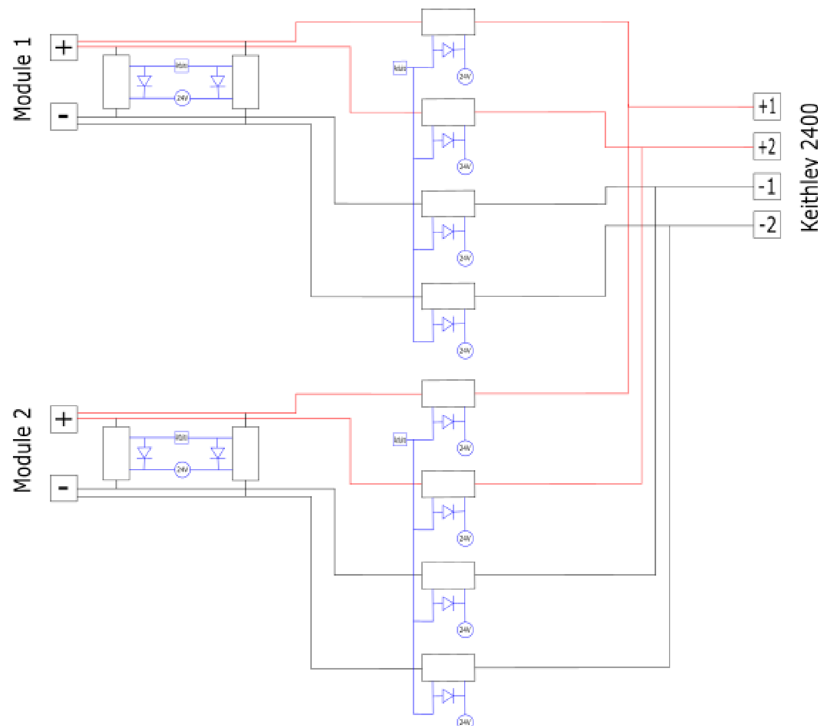

Figure 4.2: Schematic of the reed relays used to switch between the modules for measuring. The blue lines are the control of the reed relays at a voltage of 24 V, the red lines are the positive lines of the modules/K2400, and the black lines are the negative lines of the modules/K2400

4.1.3 Stress testing

The schematic of the high voltage polarity switching in the switch matrix is shown in Figure 4.3. This switching allows to mechanically disconnect the high voltage from the PV modules and invert the positive and negative poles. Four reed relays are necessary to make this switching possible. As shown in Figure 4.3, the two upper reed relays are connected to the Arduino and the lower are connected to the Arduino separately. The reason for this is that the upper reed relays and the lower reed relays should never be activated at the same time, because this shorts the HV-source. When the high voltage is turned on without being inverted, the upper two reed relays are activated. When the high voltage is turned on

and is inverted, the lower two reed relays are turned on. With the ability to switch the polarity of the HV-source, it is possible to stress and cure the modules.

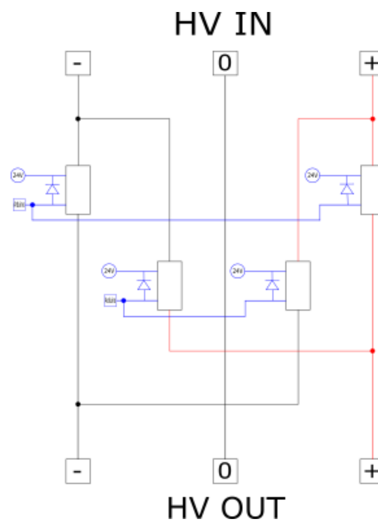

Figure 4.3: Schematic of the high voltage polarity switching. The blue lines are the control lines of the reed relays at a voltage of 24 V, the red lines that are connected to the positive high voltage output, the black lines are connected to the negative high voltage output, except the lines for the zero, this line is connected straight from input to output without any interference

4.1.4 Front panel layout

The front panel of the switch matrix is shown in Figure 4.4. In the top left, the high voltage inputs are located. Below the inputs, the high voltage outputs are located. The connections for module one up to six are located to the right of the high voltage connectors. The K2400 should be connected to the most right column of banana connectors. For one column of connectors, the upper red banana connector is used as the positive wire of the voltage, the red connector underneath is for the positive current wire. In the same row, the upper black connector is for the negative wire of the voltage, the black connector underneath is for the negative current wire. The USB cable to the laptop running the LabVIEW program and the power switch are located to the right of the panel.

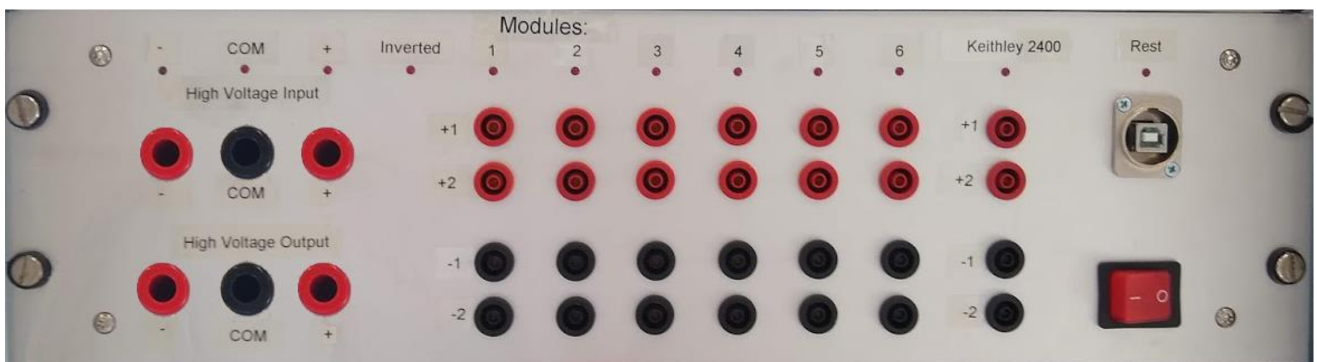

Figure 4.4: Front panel of the switch matrix

4.1.5 Low voltage electrical control

To control the reed relays, a printed circuit board (PCB) is made to provide the low voltage logic. Figure 4.5 shows the schematic of the PBC. The main part of the PCB is the Arduino Nano in the centre. The Arduino Nano communicates with the LabVIEW program via a USB connection. LabVIEW controls the Arduino to set each port high or low. With this, the right port is made high at the right time.

On the left of Figure 4.5, the connector to the LEDs on the front panel of the switch matrix is shown. On the right of Figure 4.5, the connector to the reed relays is displayed. The reed relays operate at a voltage of 24 V, the Arduino can only handle 5 V. To be able to switch the reed relays with the Arduino, a transistor circuit is used to amplify the signal from 5 V to 24 V. The diodes on the schematic are flyback diodes to eliminate any voltage peaks from the coil of the reed relay. The three two-pin connectors in Figure 4.5 are used for: 5 V and ground, two extra ground pins, and 24 V and ground.

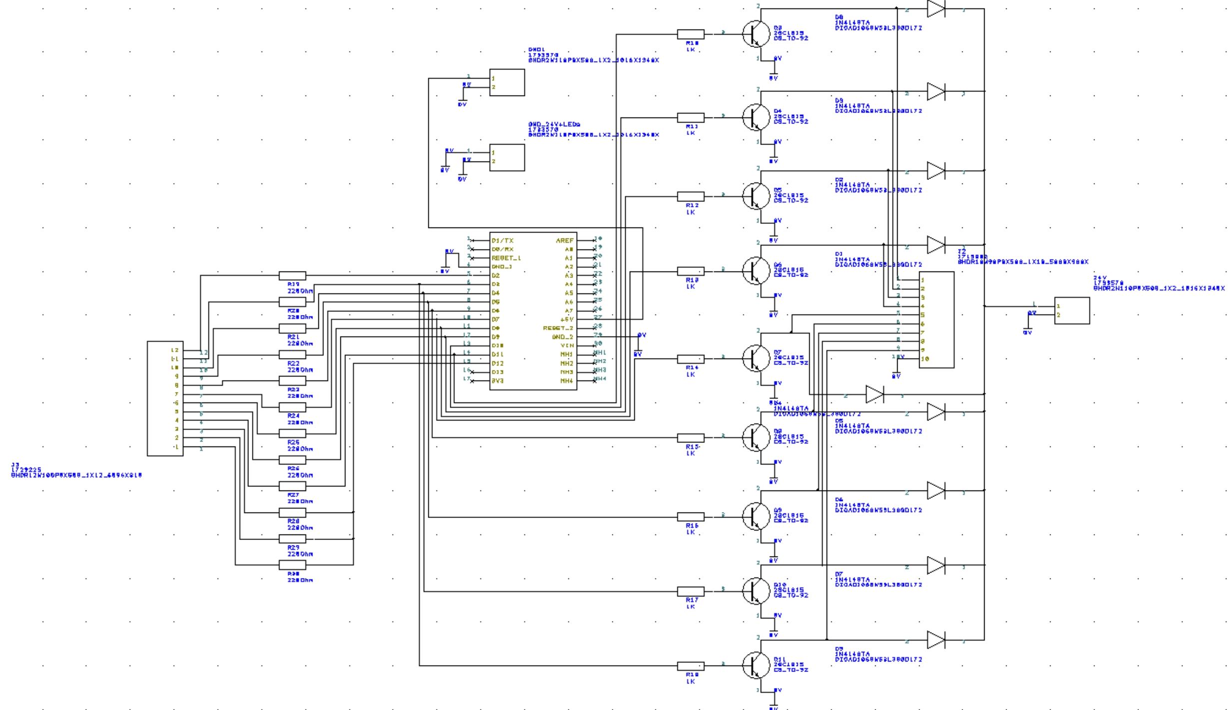

Figure 4.5: Schematic of the PCB to control the reed relays

4.1.6 Software: LabVIEW

The LabView program consists of two main tabs, shown in Figure 4.6 and Figure 4.7. The tab shown in Figure 4.6 is the main tab of the program. The second tab, shown in Figure 4.7, is the tab with all the settings for the switch matrix, high voltage source and the K2400.

The main tab has the start-, stop buttons and the pause-, resume buttons. Underneath the buttons, there are five indicators. If a measurement is in progress, the first indicator shows the module that is currently being measured. The second indicator shows the total runtime of the program, the third indicator shows the total time the HV- source was active, the fourth indicator displays the voltage of channel one of the HV-source, and the fifth indicator displays the voltage of the second channel of the HV-source.

The left graph shows the last measured IV-curve. The right graph displays the shunt resistance of the module as a function of the time. Each time a measurement is acquired, the shunt resistance is calculated, as discussed in 2.2.2, and added to a separate .csv file with the corresponding stressed time. It should be noted that this shunt resistance is an estimation and is used above all to have a reference how the PID-s changes during the stressing/curing as a function of time. Each module has its own tab with the shunt resistance graph and an indicator with the last shunt resistance value measured.

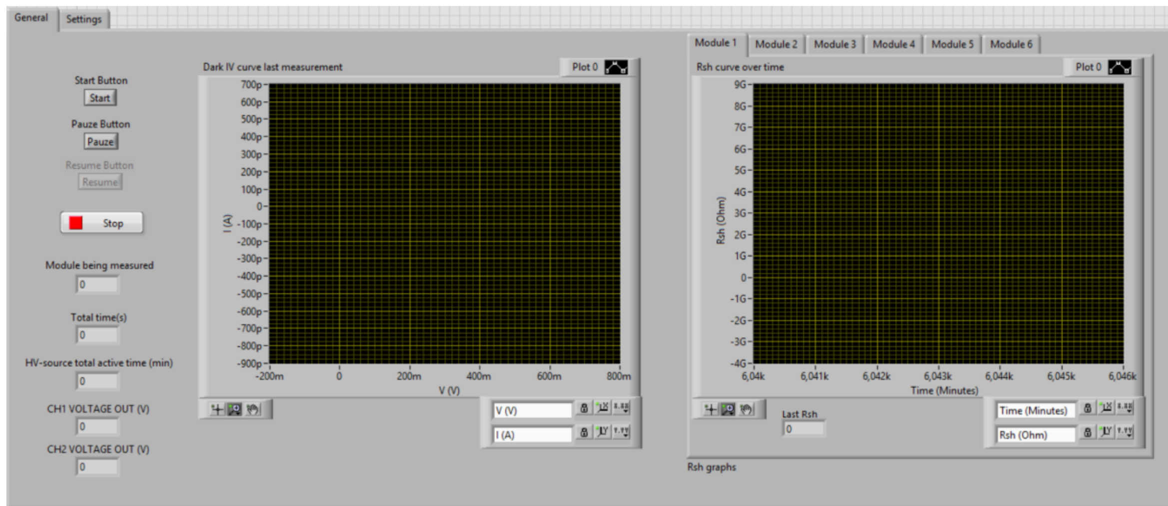

Figure 4.6: Main tab of the LabVIEW program

The necessary settings to run the setup can be adjusted in the settings tab displayed in Figure 4.7. The settings are grouped for each device. The settings for the switch matrix are on the left, the COM port, starting stressed time, polarity of the HV-source, total HV-source active time, time between measurements, number of modules to be measured, and the path to the location where the .csv files should be saved is entered here. In the second cluster, the settings of the Keithley 2400 are entered. The settings that are required are the GPIB address, the source mode, sweeping range, the number of points to be measured, and the timeout time. The last cluster contains the settings for the HV-source. The COM port of the HV-source, the mode of the source, constant voltage or constant current, the desired voltage and current for the first and second channel, and an on/off button whether this channel should be active during the time the HV-source is active is entered here. If this button is deactivated for a channel, no voltage will be over this channel. Most of the time, only one of the two channels the HV-source provides is needed, the other channel can be turned off to increase the safety of the setup.

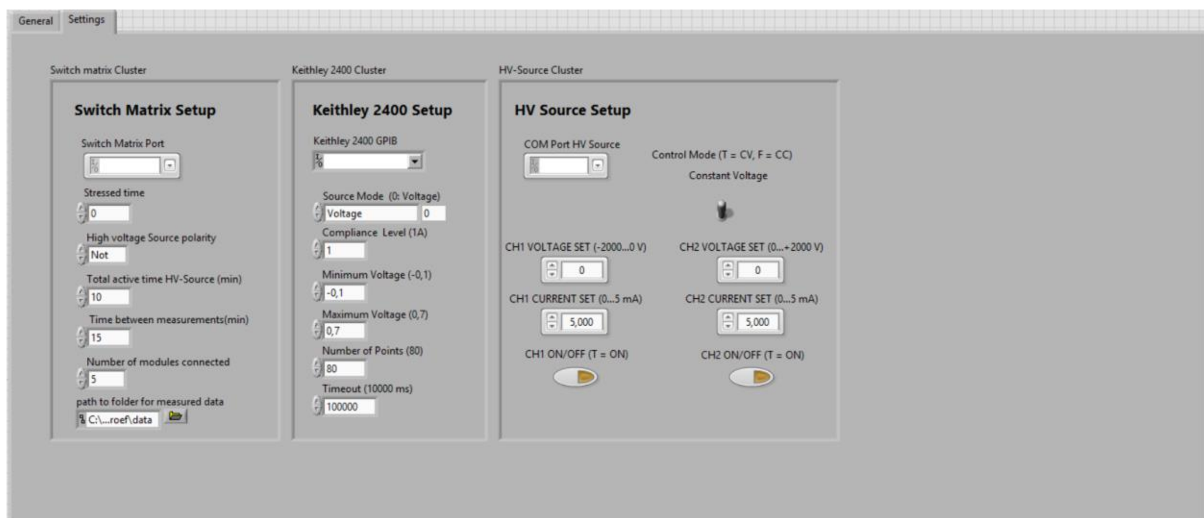

Figure 4.7: Settings tab of the LabVIEW program

4.2 Data automation with Python

4.2.1 Data processing of PV module measurements

In this Master's thesis, different devices are used to characterise the PV modules. All the data from one device needs to be assembled into one clear Excel file. To do this with Python, the openpyxl library was used. This library allows to read and write to cells, create new sheets, and generate graphs in Excel.

4.2.1.1 LOANA

The pv-tools LOANA was used for measuring the light and dark IV characteristics, as well as the EQE of the PV modules. This device generates numerous files: .lgt, .drk and .eqe, with the ligh IV, dark IV and EQE measurement data. Besides the measurement data, these files contain information about the date of the measurement, the settings of the LOANA, and measurement conditions. Furthermore, a data-exchange Excel file is created. This file contains the parameters of the sample, such as I_{sc}, V_{oc}, FF, η and more. These files are stored in a specific file hierarchy, shown in Figure 4.8.

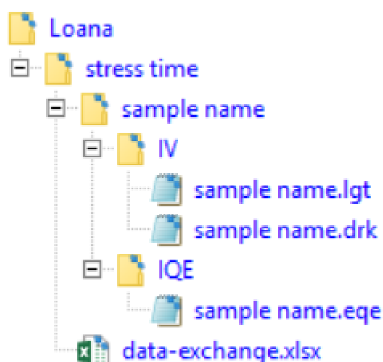

Figure 4.8: File hierarchy of LOANA files. The stress test folder (here LOANA) contains the data-exchange file and the folders of different stress times. These folders contain all the measured samples. The sample folders contain an IQE folder, with the EQE data in the .eqe file, and an IV folder, with the light and dark IV data in the .lgt and .drk files respectively

The custom-made Python program finds these files in the right location and stores the data together in an Excel file. A sheet is created for every sample with the light and dark IV data and graphs. This sheet also contains a table with the sample parameters from the data-exchange file and the calculated PID percentage. The PID percentage is calculated with the following equation:

$$\%PID = 1 - \frac{\eta(t_n)}{\eta(0)} \tag{9}$$

Another sheet is generated for each sample with the EQE data and calculated normalized EQE. Graphs of both EQE and normalized EQE are generated. Figure 4.9 shows an example of the generated graphs of one sample.

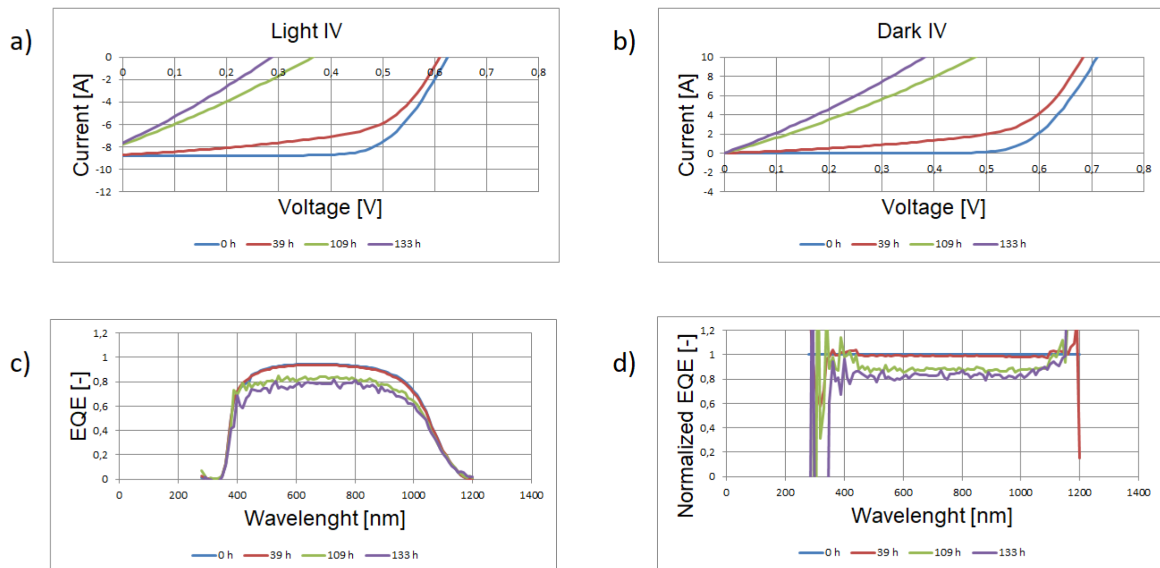

Figure 4.9: Generated graphs of one sample of (a) light IV, (b) dark IV, (c) EQE and (d) normalized EQE

Another four graphs are created to compare the samples with each other: PID percentage as a function of stress duration, FF percentage as a function of PID percentage, V_{oc} as a function of PID percentage, and I_{sc} as a function of PID percentage. Figure 4.10 shows an example of these graphs. This way, the data can be easily interpreted.

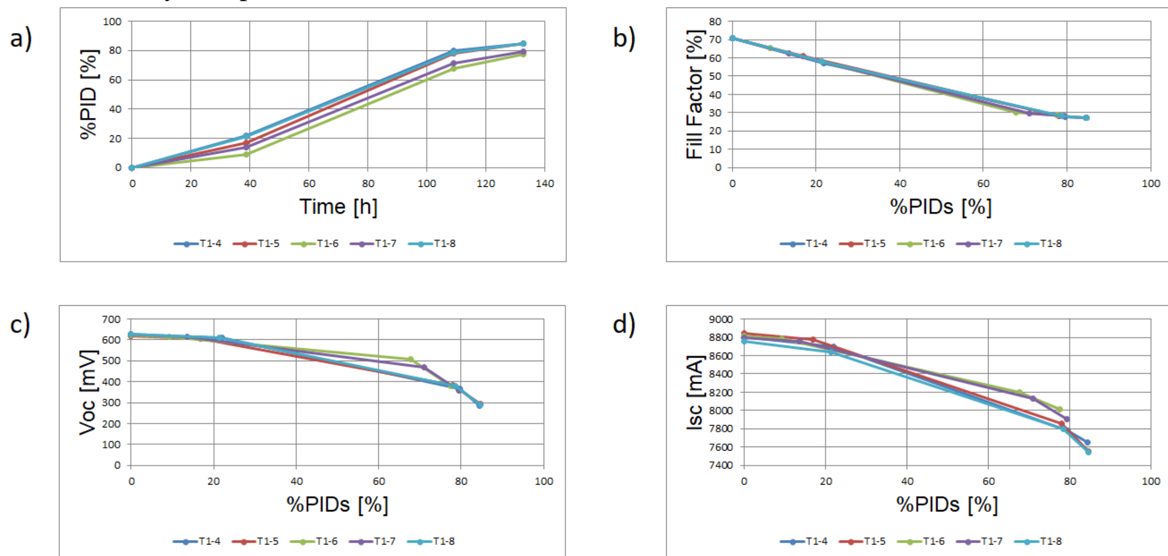

Figure 4.10: Generated graphs of all samples of (a) %PID, (b) %FF, (c) Voc and (d) Isc

The stress time folders are manually set in the LOANA software. Because the times are not always correctly set, the Python program calculates the stress times exactly. To do this, five columns, ‘Date’, ‘Time (out)’, ‘Time (in)’, ‘Interval [h]’ and ‘Acc. Hours [h]’, need to be present in an Excel sheet with the name ‘General’. It is important that these columns are in this order and in columns A through E. The row does not matter. In column A, the date is filled in by the user (format dd:mm:yyyy). In column B, the time is filled in, by the user, when the stress test pauses (format hh:mm). In column C, the time is filled in, by the user, when the stress test resumes (format hh:mm). In column D, the interval between two stress test pauses is displayed in hours. This is calculated by the Python program. In column D, the total stress duration in hours is displayed. This is also calculated by the Python program. These calculated hours are then used in the graphs to ensure the correct presentation of the PID process.

A	B	C	D	E
Stress duration				
Date	**Time (out)**	**Time (in)**	**Interval [h]**	**Acc. Hours [h]**
22/05/2019		16:45		0,00
24/05/2019	9:48	11:57	22,10	38,87
27/05/2019	10:22	15:51	70,42	109,28
28/05/2019	15:15	16:46	23,40	132,68

Figure 4.11: General sheet with the five necessary columns. In column A, the date is filled in (format dd:mm:yyyy). In column B, the time is filled in when the stress test pauses (format hh:mm). In column C, the time is filled in when the stress test resumes (format hh:mm). In column D, the interval between two stress test pauses is displayed in hours. This is calculated by the Python program. In column D, the total stress duration in hours is displayed. This is calculated by the Python program

4.2.1.2 PME

Light IV measurements of thin film modules are saved in .dat files, which also need to be collected into one clear file. Other data, such as the open circuit voltage, fill factor and efficiency are stored in .ini files. The names of these .dat and .ini files need to have the format: sample name - number of stressed minutes - sample number - measurement number. The thin film files are all saved together in one folder. The file structure is shown in Figure 4.12.

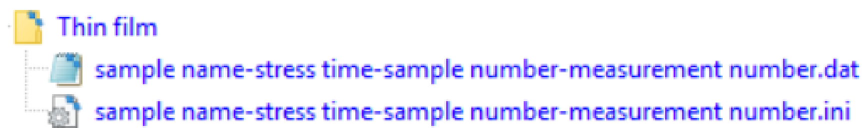

Figure 4.12: File hierarchy of thin film files. One folder of the stress test (here Thin film) contains all the files of all the samples for all the stress durations

Every sample with sample number and measurement number is parsed to one sheet in the Excel file. This sheet contains the light IV measurement data with the IV graph, similar to Figure 4.9a. A %PID sheet is also generated with a graph containing the PID percentage of all the samples as a function of the stress duration, similar to Figure 4.10a.

4.2.1.3 K2400

The switch matrix with the LabVIEW program was used to measure the dark IV characteristics of PV modules *in-situ*. The switch matrix measures the PV modules after a certain number of minutes and saves the data on the computer. This data is organised on the computer in a specific way. Each module under stress has a folder with its name. In this folder, the dark IV data is stored. These .csv files are named after the number of minutes of stressing since the start of the program. It also contains the R_{sh} .csv file. This contains the value of the R_{sh} of each dark IV measurement. The file structure is shown in Figure 4.13.

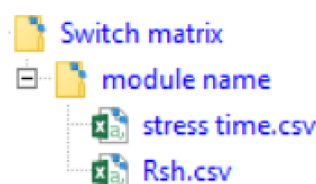

Figure 4.13: File hierarchy of switch matrix files. In the stress test folder (here Switch matrix), a folder is located for each module under stress. These folders contain the measurement data of all stress durations and the R_{sh} file

The Python program collects the data for all PV modules, for all minutes, and assembles it all in one Excel file. This file consists of several sheets, one for each PV module. In this sheet, the dark IV data is arranged from the first measurement through the last. The program also generates a graph of the data, similar to Figure 4.9b. A sheet with all the R_{sh} values of each module at each time is created. The shunt resistances of each module as a function of the stress duration is visualised in a graph, an example is shown in Figure 4.14.

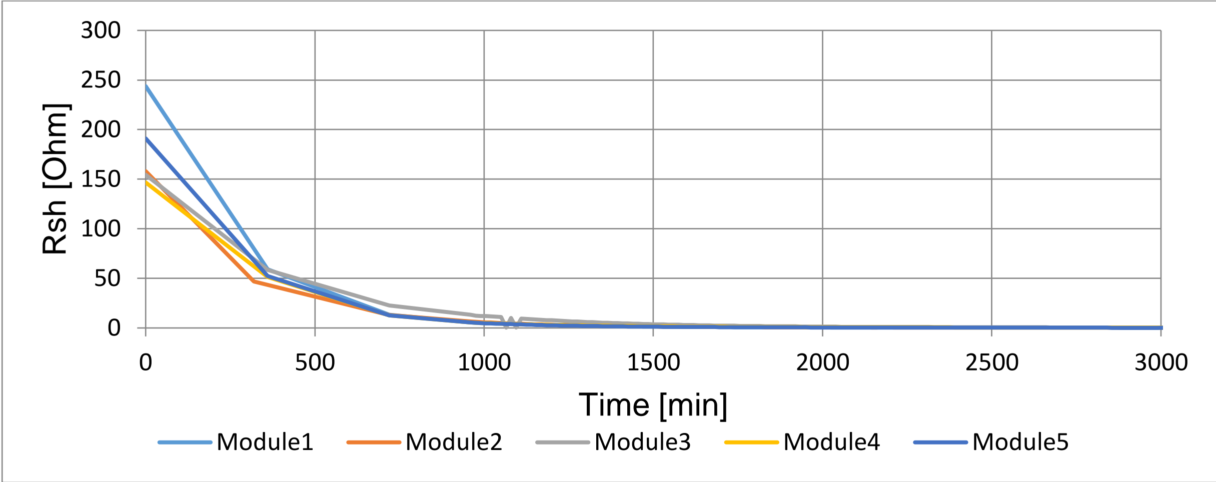

Figure 4.14: Graph of R_{sh} values of each module

4.2.2 Combine EL-photos of PV-laminates

The Python Image Library (PIL) is used to put all the EL-photos together in one .jpg image, with the sample names and stress times on the left and on top of the images respectively. The OpenCV and Numpy libraries are used to first transform the EL-photos into a square. This is achieved by first detecting the edges of the samples and then finding the corners. These corners are then used to form a square image. This way, no black borders are present in the resulting image. Figure 4.15 shows an example of a resulting image for two samples and two stress durations.

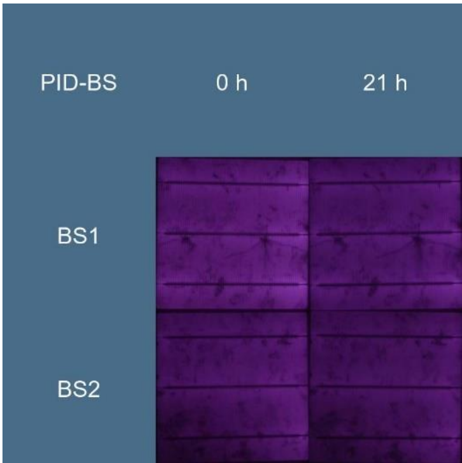

Figure 4.15: Resulting image of EL-photos. On the right, the sample names are mentioned. On top, the stress duration is displayed. In the top left corner, the stress test name is displayed

4.2.3 Graphical User Interface of data processing program

A GUI was made to easily operate the program. The TkInter library was used to achieve this. The interface consists of two tabs: processing and info. Figure 4.16 shows the processing tab. The user is able to select a few options before running the program. First, the device with which the data is obtained is selected. Three options are available: LOANA, PME and K2400. Then, the stressing duration is

chosen. If ‘All’ is selected, all the stressing data is combined in the Excel file, however, an interval can be selected when necessary. If the user only wants data with at least a certain amount of time in between, the ‘Data every …’ checkbox is checked. Furthermore, an Excel file is chosen in which the data is saved. Finally, the user is able to choose which data to save: IV, EQE or EL picture. Multiple options are possible, however, these options are only available if LOANA is selected, because thin film and switch matrix only have IV data. When everything is correctly selected, the begin button is pressed. The label on the left of the button displays the current state of the program. It gives an error message if something is not filled in correctly, for example if the selected file is not an Excel file. Furthermore, when the program is running, it displays the message: ‘Running…’. Finally, when the program is done, it displays ‘File saved’.

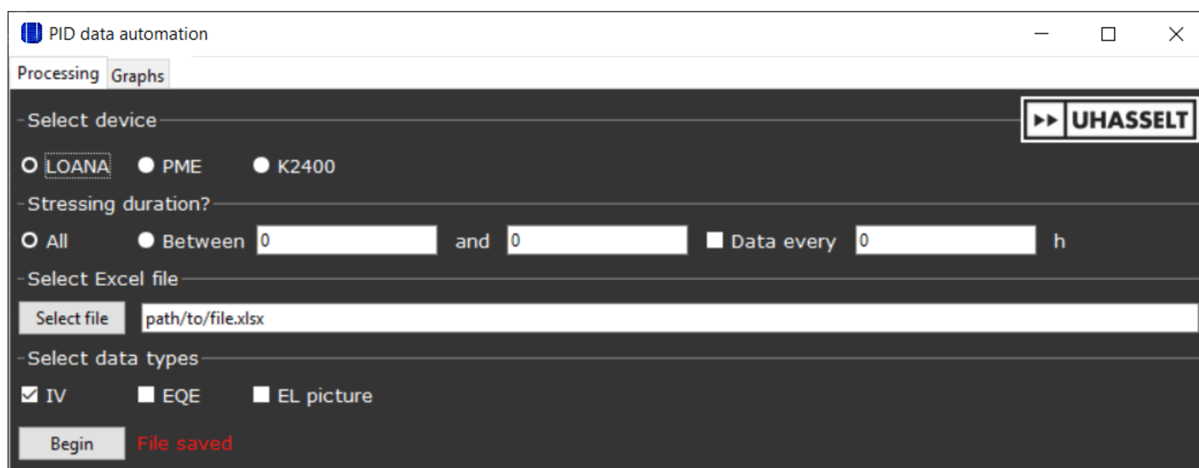

Figure 4.16: Processing tab. On top, radio buttons of different measurement devices are present. The stressing duration which needs to be processed can be controlled. An Excel file is selected with the ‘Select file’ button. Three checkboxes can be checked to choose which data needs to be processed. With the begin button, the program is run

The graph tab, shown in Figure 4.17, is used to plot the IV graphs. This way, the user is able to immediately inspect the curves. After the user has processed data in the processing tab, the names of the modules appear in the graph tab. After a sample is selected, the graphs are displayed when the begin button is pressed. A table with the evolution of the parameters %PID, I_{sc}, V_{oc} and FF is shown on the right side. For K2400, only R_{sh} is shown. With the toolbar below the graphs, the user is able to zoom in on the graph and save it on the computer.

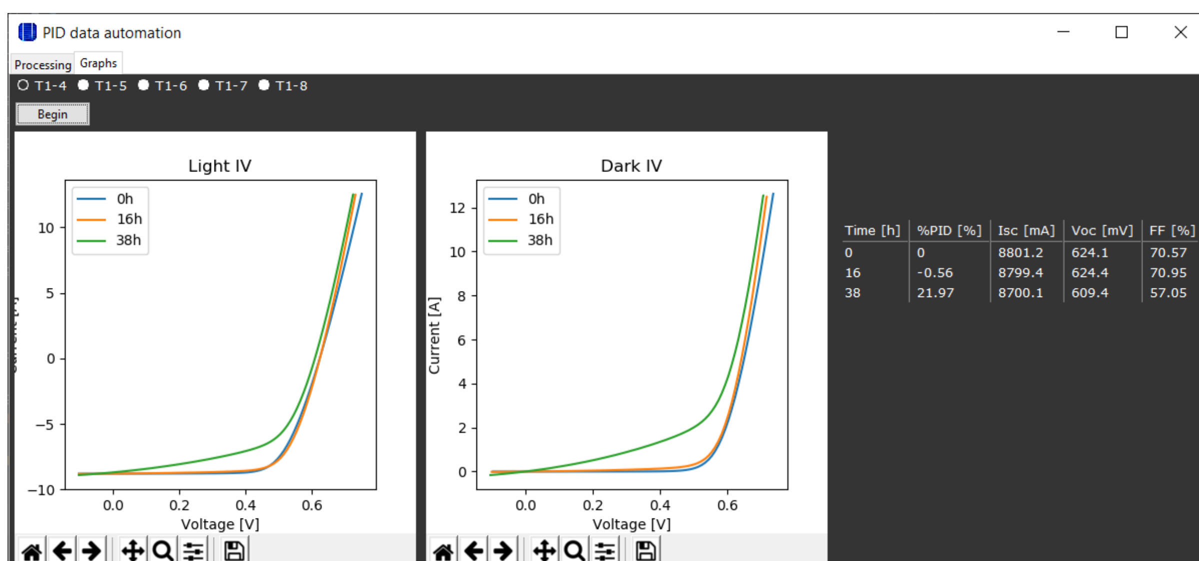

Figure 4.17: Graphs tab. On top, radio buttons of all the sample names are present. When the begin button is pressed, IV curves are shown and on the right side, a table with the evolution of a few parameters of the chosen sample is shown

5 PID-s test with switch matrix

The switch matrix and the associate setup are tested with five monofacial multi crystalline PV modules. First, these modules are stressed to induce PID-s. After these modules have a copious amount of PID-s, they are cured to test the inverted high voltage mode of the switch matrix. The results of these tests are post-processed with the custom-made Python program to verify the performance of the software.

5.1 Experimental

Five monofacial multi crystalline Al-BSF PV laminates are stress tested to induce PID. Figure 5.1 shows one of the laminates, the others are identical to this one. The cells are laminated with an EVA encapsulant between a 2 mm thick soda-lima glass on the front and a backsheet on the back.

The frame and foil methods, explained in 2.3.2, are used together to enhance the PID stressing process. The laminates are stressed with a voltage of 2000 V between the cell and the aluminium foil, on a temperature of 60°C. The cell is negatively polarized relative to the aluminium foil. After more than 100 hours of stressing, the laminates are cured by reversing the voltage polarization. This means that the cell is positively polarized relative towards the aluminium foil.

The PID process is mapped by measuring the dark IV curve every 15 minutes with the use of the switch matrix. Furthermore, light IV characteristics are measured regularly with the LOANA.

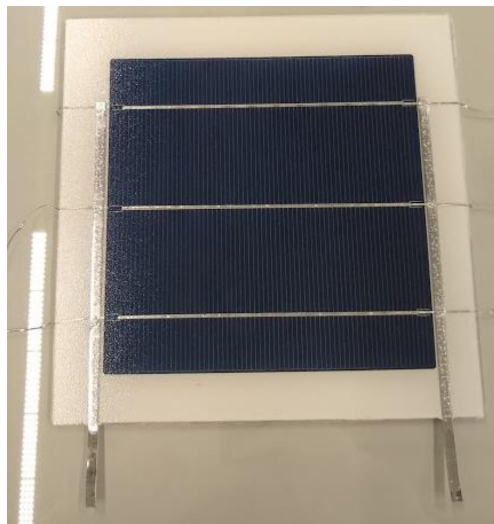

Figure 5.1: PV-laminate

5.2 Results

First, the samples were stressed for 119 hours. Figure 5.2a shows the graph of the PID percentage as a function of the stress duration. The %PID increases for all the samples similar during the stress test. The R_{sh} values from all samples are shown in Figure 5.2b. R_{sh} decreases during the stress test, as the %PID increases. This change of R_{sh} is also the same for all samples.

Figure 5.2c shows the EL images of the samples at different stress durations. The EL images show that the emitted light decreases in strength over time. The samples all show similar decreases of emitted light.

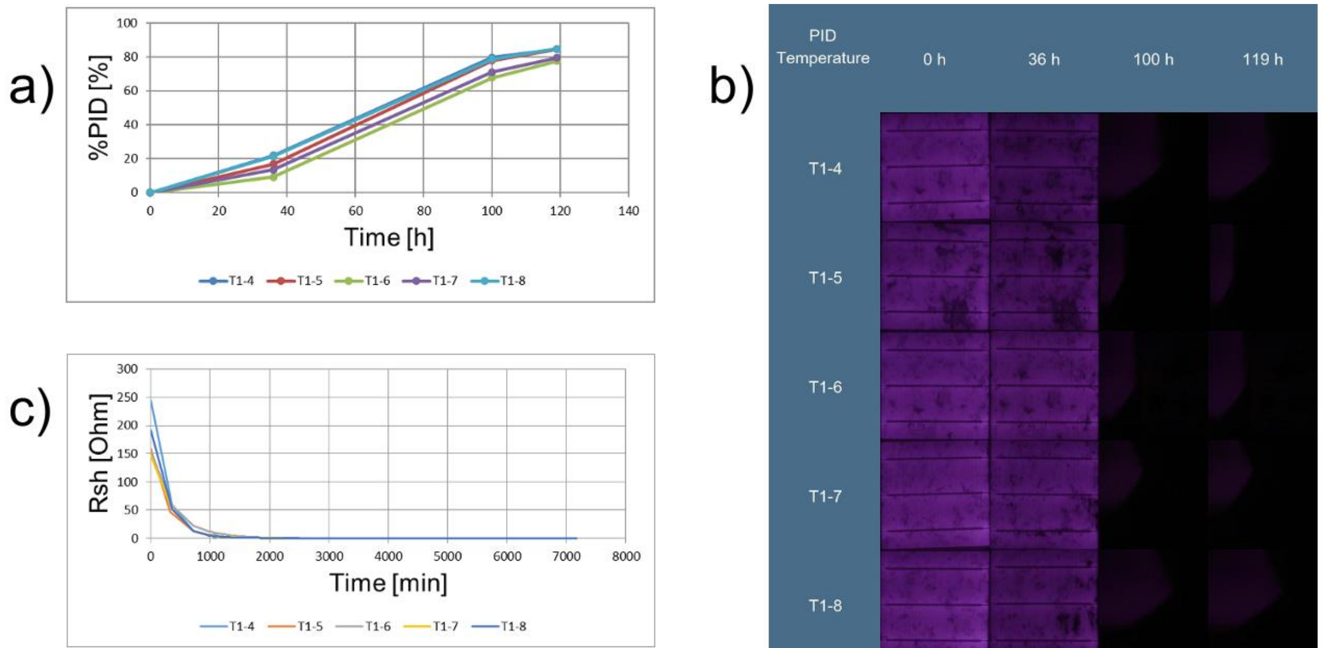

Figure 5.2: Comparison of the samples after stressing. (a) %PID as a function of the stress duration of all the samples (b) R_{sh} of every sample as a function of stress duration (c) EL-images of all the samples at different stress times

Because the samples are so similar, the data discussed in this section originate all from the sample T1-4 laminate. This sample is chosen because it has the highest %PID after stressing. The dark IV measurements, obtained from the switch matrix setup, is shown in Figure 5.3. This graph shows data from 0 hours up to 63 hours of stressing. A dark IV measurement was done every 15 minutes. The PID process is observed. The slope of the graph is increasing with each measurement, because of the decreasing R_{sh}. The blue arrow indicates the direction the graph shifts through the stressed time. However, this graph is to crowded to be legible. Furthermore, Excel can only manage up to 250 measurements in one graph. For this reason, the data is filtered to show a measurement every 6 hours instead of every 15 minutes.

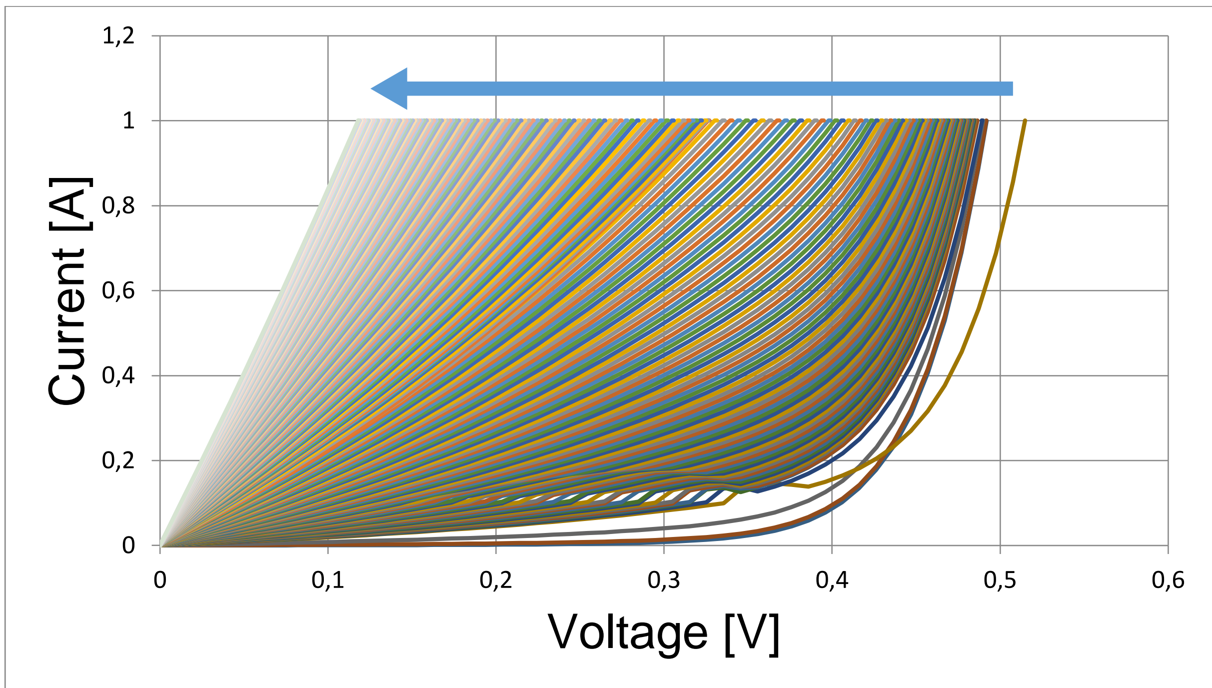

Figure 5.3: Dark IV data of one sample obtained from the switch matrix setup. All measurements from 0 hours up to 63 hours of stressing are present. The blue arrow indicates the direction the graph shifts through the stressed time

The filtered dark IV measurements are shown in Figure 5.4. Because less measurements are displayed, the graph can show until 120 hours of stressing. Because of the filtering, this graph is more readable than Figure 5.3. In this graph, the decrease of R_{sh} is observed, as well as the rate of the PID process. The blue arrow indicates the direction the graph shifts through the stressed time.

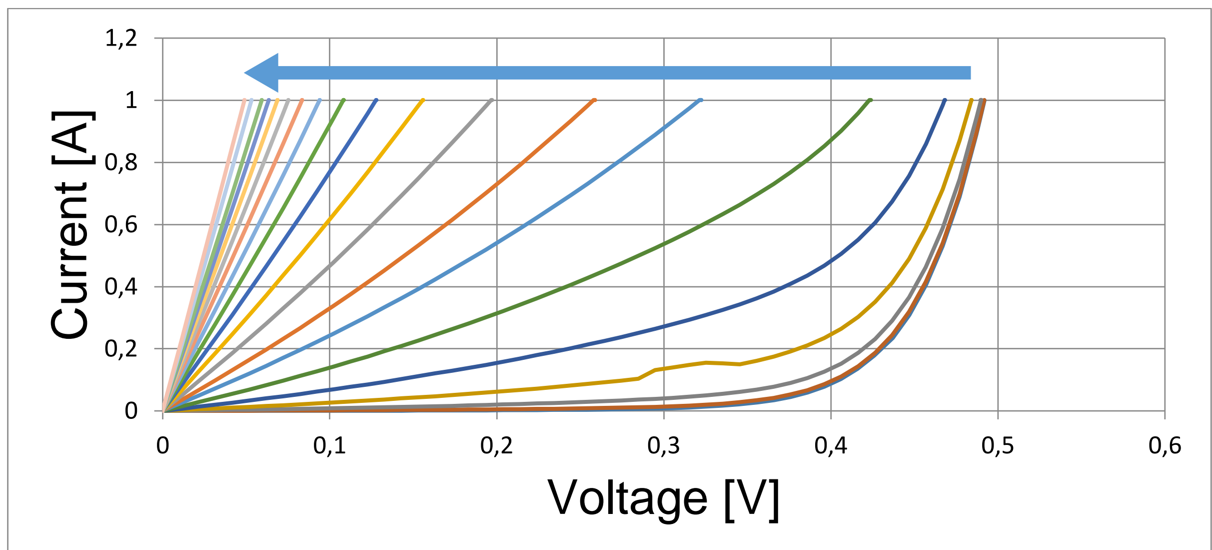

Figure 5.4: Dark IV data of one sample obtained from the switch matrix setup. The graph has measurement data of every 6 hours instead of every 15 minutes. It contains measurements from 0 hours up to 120 hours of stressing. The blue arrow indicates the direction the graph shifts through the stressed time

From these dark IV measurements, the R_{sh} is calculated. The R_{sh} as a function of the stress duration is shown in Figure 5.5. It is observed that the R_{sh} decreases significantly in the first 1000 minutes of stressing. After that, it converges slowly to 0.

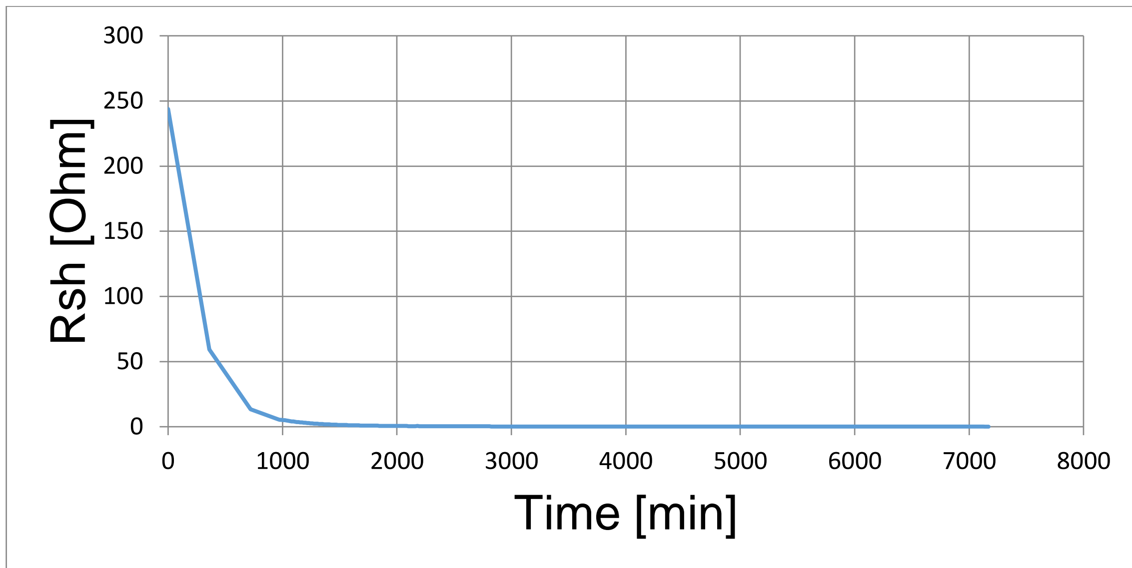

Figure 5.5: R_{sh} as a function of stress duration

The light IV characteristics were measured at several times during the stress test. In Figure 5.6, the light IV curve is shown. It is observed that the V_{oc} decreases drastically while I_{sc} stays relatively the same. The increase of the slope at I_{sc} indicates the decrease of R_{sh}. The increased slope results in a reduction of the FF.

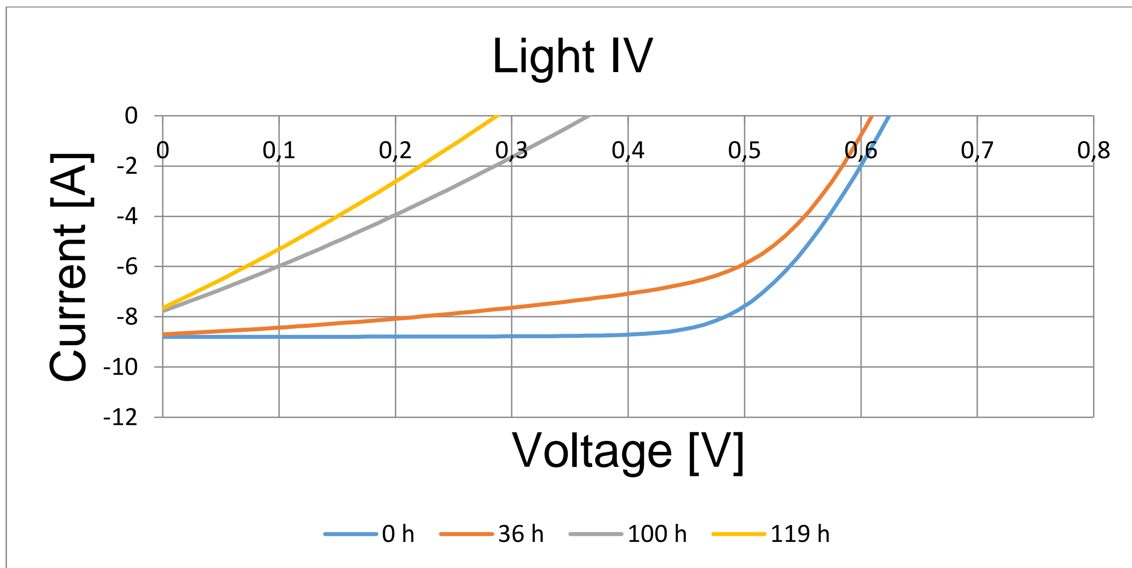

Figure 5.6: Light IV curve of T1-4

The values of the cell parameters are shown in Table 5.1. As observed in the graph, V_{oc} decreases significantly, while I_{sc} stays relatively the same. The efficiency decreases drastically, as well as the FF. The PID is increased from 0% to 84,5% after 119 hours of stressing.

Table 5.1: Cell parameters before and after stressing

Time [h]	*Efficiency [%]*	*Isc [mA]*	*Voc [mV]*	*FF [%]*	*%PID [%]*
0	15,93	8801,2	624,1	70,57	0
36	12,43	8700,1	609,4	57,05	21,97112
100,58	3,247	7775,8	365,9	27,78	79,61707
119,25	2,468	7653,3	287,4	27,31	84,50722

The PID percentage as a function of stress duration is shown in Figure 5.7. It is observed that the PID increases as the stress duration increases. This graph forms an S-shape. At first, the PID increases significantly. However, after, 110 hours, the PID rate decreases.

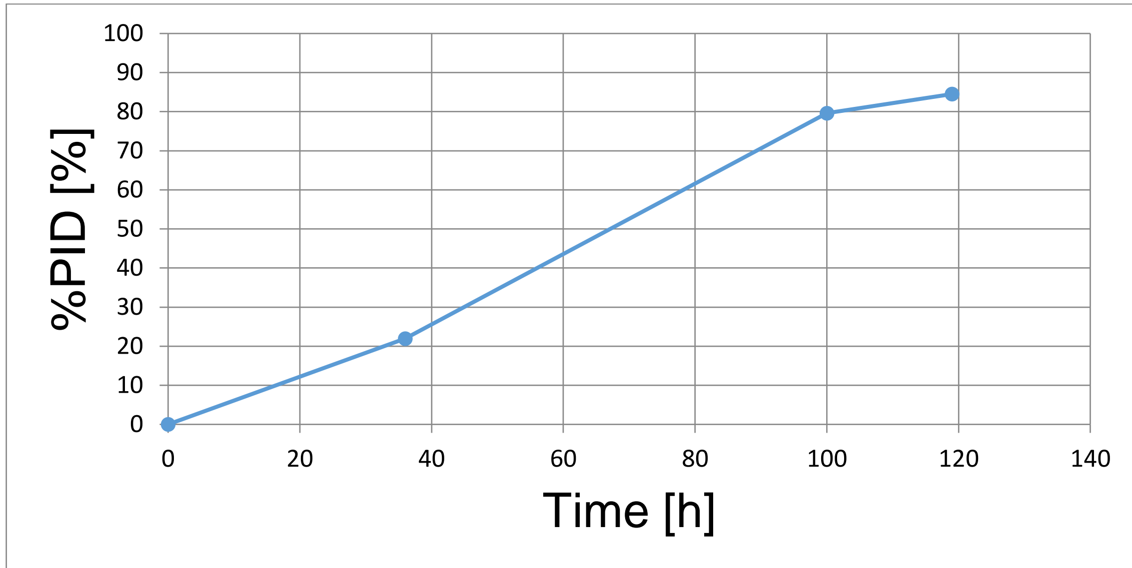

Figure 5.7: PID percentage as a function of stress duration

The EL images of the sample are shown in Figure 5.8. The brightness is decreased after 36 hours of stressing. A few new dark spots are also noticed between 36 hours of stressing and before stressing. This indicates PID-s. After 100 hours of stressing, the sample does not emit any EL light anymore, indicating the module has degraded so much that no EL light can be observed anymore.

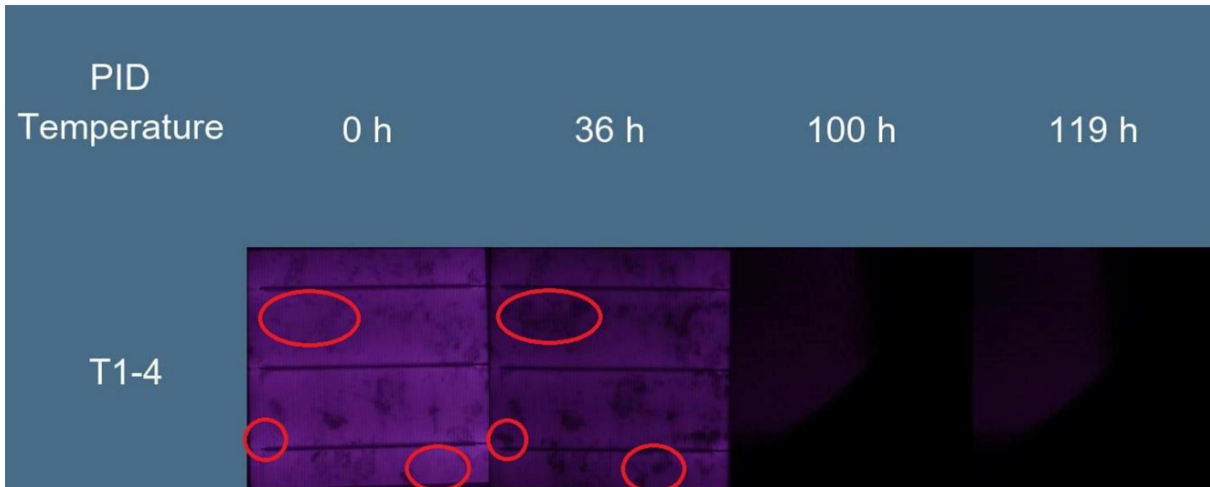

Figure 5.8: EL images at different stress durations. The brightness of the images decreases over time. After 100 hours of stressing, the images are completely dark. New dark spots after stressing indicate PID-s

As discussed in 2.3.3.1.2, the power at 25°C can be calculated from the dark IV measurements at stress temperature. With the use of equations (6), (7) and (8), the dark IV derived power at 25°C is calculated. The normalized dark IV derived power at 25°C correlates to the normalized light IV derived power at 25°C. Figure 5.9 shows the y = x relation. The normalized light and dark IV derived power are calculated for 36, 100 and 119 hours.

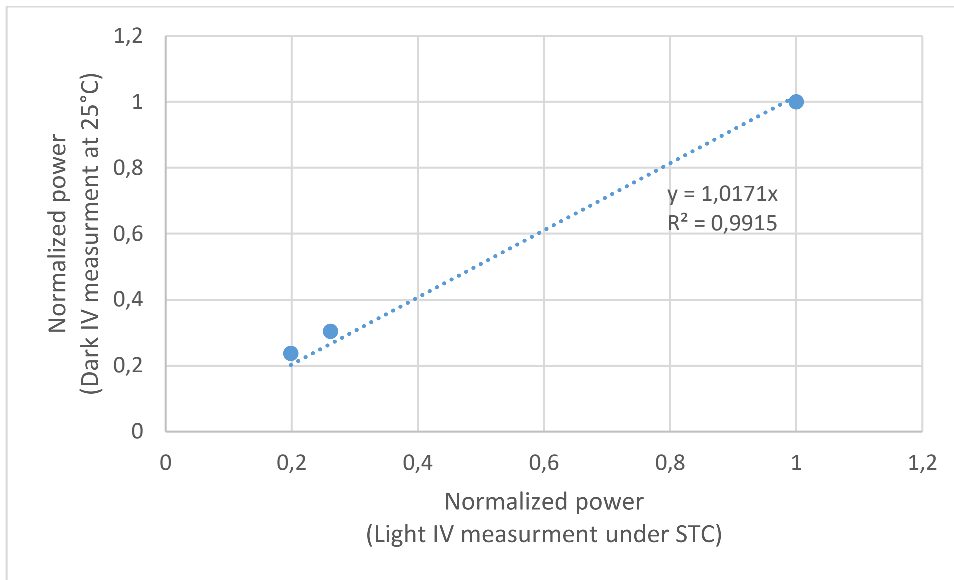

Figure 5.9: Normalized dark IV derived power at 25°C as a function of the normalized light IV derived power under STC

To calculate the dark IV derived power at a certain stress time, the dark IV derived temperature coefficient γ is calculated with equation (8) for two stress times. Here, 36 hours and 100 hours are chosen because the dark IV at stress temperature was measured for these times.

$$\frac{-2{,}3338}{-3{,}1426} = 1 + \gamma(36h)(60 - 25)$$

$$\frac{-0{,}43559}{-0{,}95553} = 1 + \gamma(100h)(60 - 25)$$

The dark IV derived temperature coefficients are: γ(36h) = -0,007353 and γ(100h) = -0,015547. Now, with the use of equation (7), the estimated k value is calculated:

$$k_{estimated} = \left(1 - \frac{-0{,}015547}{-0{,}007353}\right) / \left(1 - \frac{-0{,}43559}{-2{,}3338}\right) = -1{,}3701$$

Then, the dark IV derived power at 25°C of a stress time can be calculated with equation (6). Here, 119 hours is chosen because the light IV characteristics are measured for this stress time, thus, the calculated power can be compared to the actual value.

$$P_{dark}(25°C, 119h) = \frac{-0.33544}{1 + \left(1 - (-1{,}3701)\left(\frac{-0{,}33544}{-2{,}3338}\right)\right)(-0{,}007353)(60 - 25)} = -0{,}761113$$

With equation (6), the calculated dark IV derived power at 25°C for 119 hours of stressing is -0,761113 W. The actual dark IV derived power, measured at 25°C is equal to -0,74571 W. The difference between the actual value and the calculated value is negligible.

After, the samples were stressed for 119 hours, they were cured for 10 hours. Figure 5.10a shows the graph of the PID percentage as a function of the stress duration. The %PID decreases for all the samples similar during the curing test. The R_{sh} values from all samples are shown in Figure 5.10b. R_{sh} increases during the curing test, as the %PID decreases. This change of R_{sh} is appears different for the samples,

because they converge to different values. However, in comparison to the R_{sh} of approximately 200 before the stress test, this difference is negligible.

Figure 5.10c shows the EL images of the samples at different stress durations. The EL images show that the emitted light increases after curing. The samples all show similar increase of emitted light.

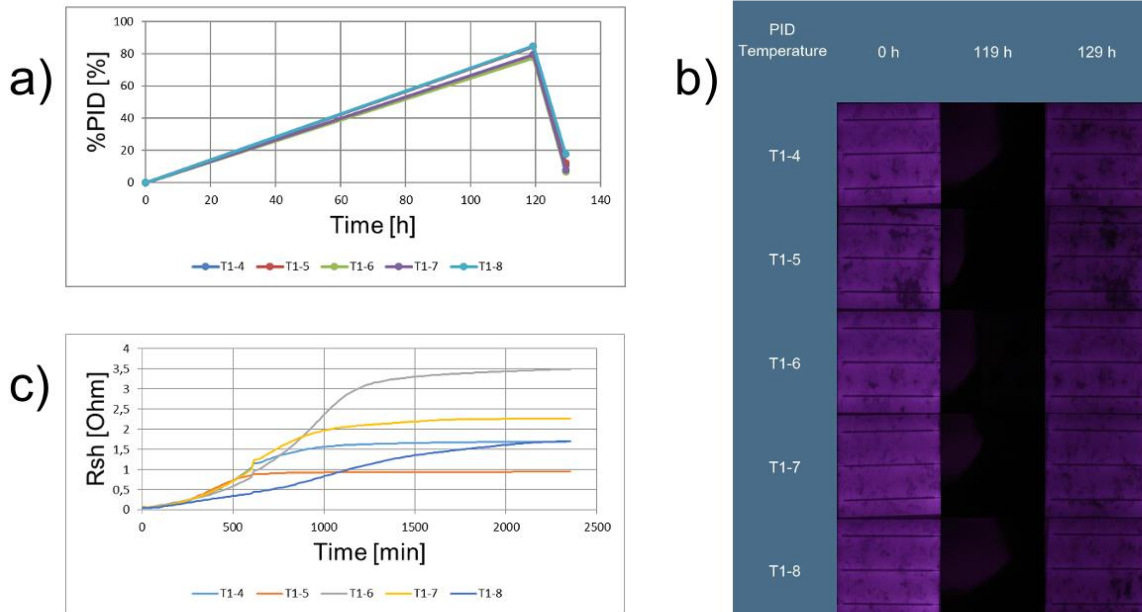

Figure 5.10: Comparison of the samples after curing. (a) %PID as a function of the stress duration of all the samples (b) R_{sh} of every sample as a function of stress duration (c) EL-images of all the samples at different stress times

Because the samples are so similar, the data discussed in this section originate all from the sample T1-4 laminate. This sample is chosen because it was also used previously.

Figure 5.11 shows a graph of the dark IV data obtained from the switch matrix setup. Measurement data every 15 minutes is shown from 0 hours up to 53,5 hours of curing. In this graph, the increase of R_{sh} is observed, as well as the rate of the PID curing process.

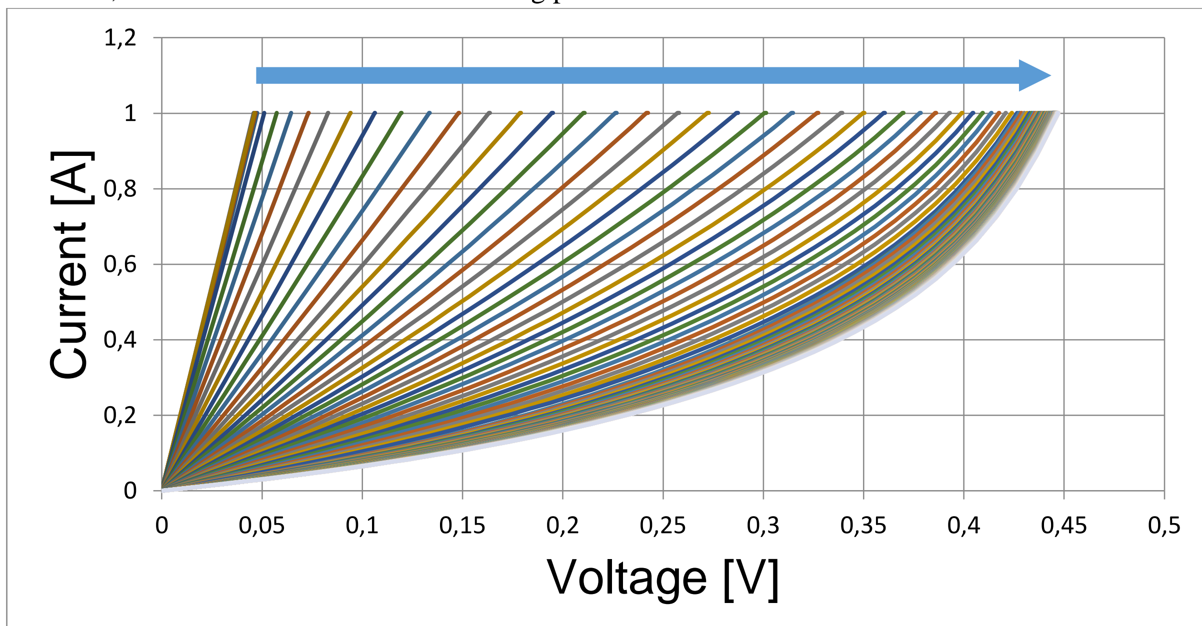

Figure 5.11: Dark IV data obtained from the switch matrix setup. All measurements from 0 hours up to 53,5 hours of curing are present. The blue arrow indicates the direction the graph shifts through the stressed time

Figure 5.12 shows the R_{sh} as a function of the curing duration. It is observed that the R_{sh} increases as a logistic function.

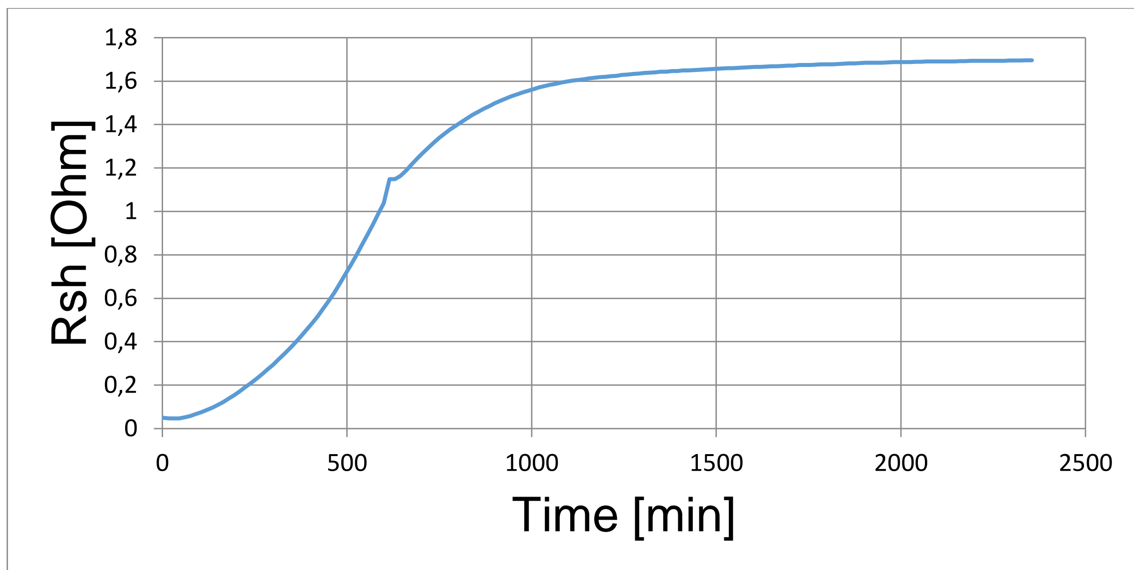

Figure 5.12: R_{sh} as a function of curing duration

Figure 5.13 shows the percentage PID as a function of the stress duration. The PID decreases significantly after curing. The PID decreases from approximately 80% to 10% in only 10 hours.

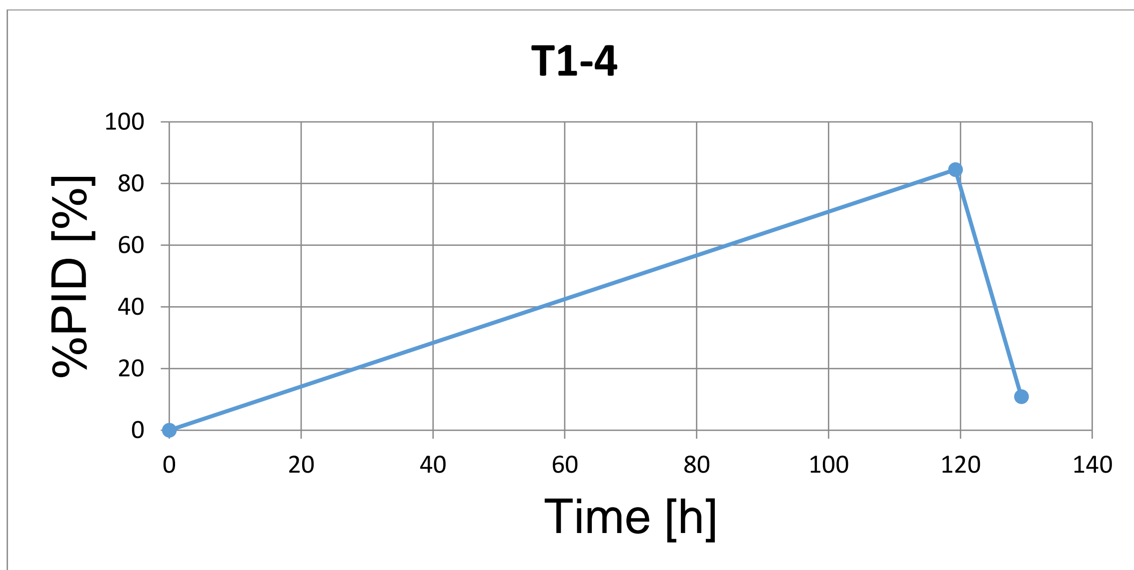

Figure 5.13: %PID as a function of the stress duration. From 0 to 119 hours the sample was stressed. From 119 hours to 129 hours the sample is cured

Figure 5.14 shows the light IV curve of the sample. It is observed that the R_{sh} is decreased after 119 hours of stressing. After 10 hours of curing, the R_{sh} is significantly increased. After curing V_{oc} increases drastically while I_{sc} stays relatively the same.

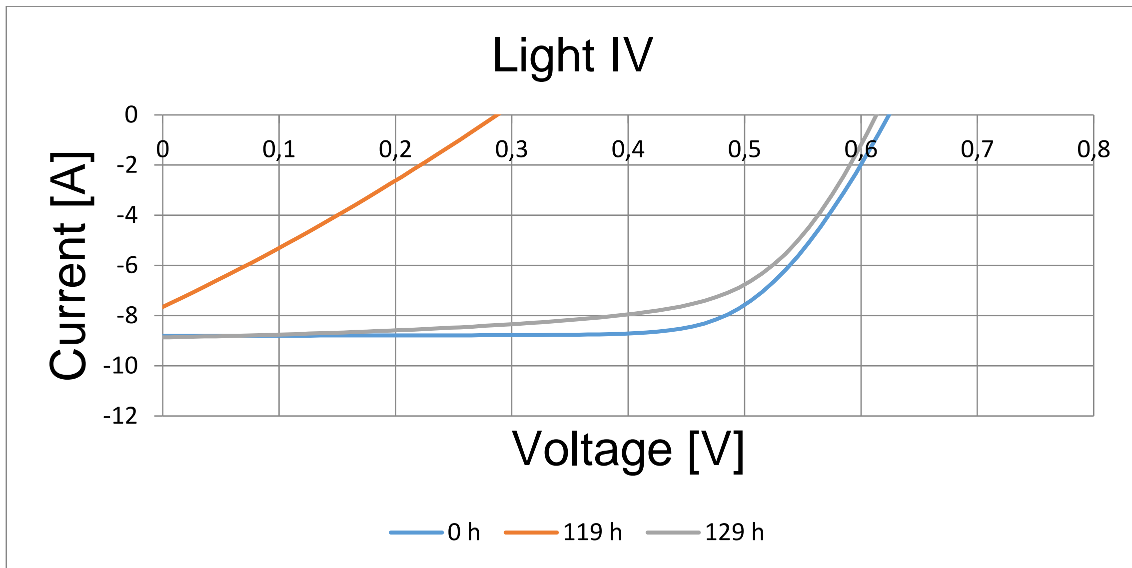

Figure 5.14: Light IV curve before stressing, after stressing and after curing

Table 5.2 shows the evolution of the cell parameters. It is observed that the efficiency decreases drastically after 119 hours of stressing and increases significantly again after 10 hours of curing, as well as the FF. I_{sc} stays relatively the same while and V_{oc} first decreases while stressing and then increases again when the sample is cured.

Table 5.2: Cell parameters before stressing, after stressing and after curing

Time [h]	Efficiency [%]	Isc [mA]	Voc [mV]	FF [%]	%PID [%]
0	15,93	8801,2	624,1	70,57	0
119,25	2,468	7653,3	287,4	27,31	84,50722
129,25	14,2	8866,5	613,2	63,54	10,86001

Figure 5.15 shows the EL images of the samples at different stress times. After 119 hours of stressing, the images are completely dark. After 10 hours of curing, the brightness is increased. However, the brightness is still lower than before stressing. A few dark spots have disappeared, while others are still present after curing. Thus, the PID-s is still present, however, an improvement is observed.

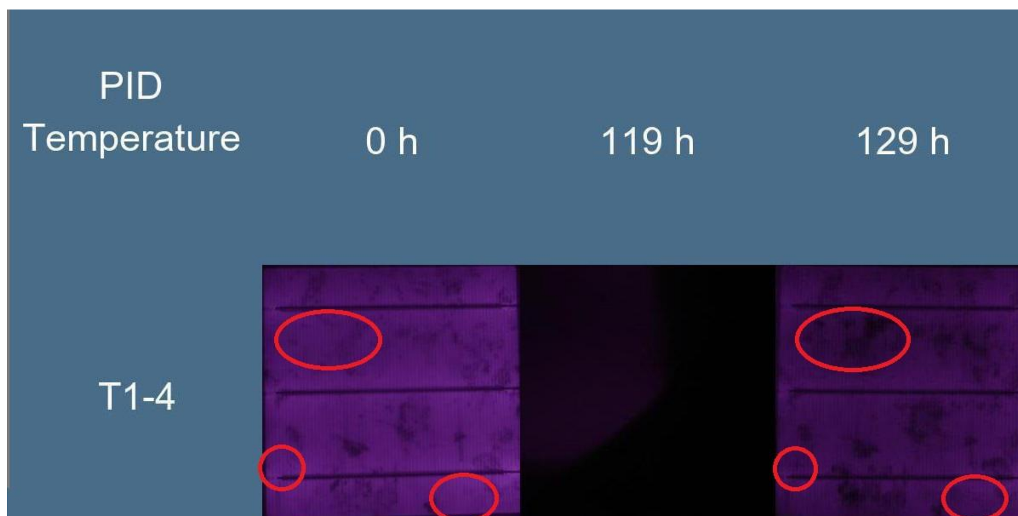

Figure 5.15: EL images at different stress durations. The brightness of the images decreases over time. After 119 hours of stressing, the images are completely dark. After curing, the brightness increases again. New dark spots are still present, indicating PID-s

5.3 Discussion and conclusion

The switch matrix measures the dark IV curve of the samples under stress every 15 minutes. However, a graph with all the measurements is not legible. Therefore, the data is filtered and processed with the custom-made Python program. At a few times during the stress test, light IV measurements are done with the LOANA. The Python program is also used to process this data. From these measurements, the cell parameters are obtained and the PID percentage is calculated. It is observed that the PID-s progresses in the samples. Therefore, it can be concluded that the switch matrix, controlled by the custom-made LabVIEW program, stresses and measures the samples correctly.

Furthermore, the equations discussed in 2.3.3.1.2 are used to convert the dark IV derived power at stress temperature measured with the K2400 to the light IV derived power at STC. It is concluded that the custom-made software and hardware for the switch matrix setup operates correctly, as well as the software for the data processing.

The samples are also cured after the stress test with the switch matrix in inverted mode. The dark IV curves are also measured every 15 minutes. After 10 hours of curing, light IV measurements are done with the LOANA. It is observed that the PID percentage is decreased drastically. It is concluded that the inverted mode of the switch matrix operates correctly as well.

6 Conclusion

PID reduces the efficiency of PV modules drastically. Thus, preventing PID is desired to obtain the best possible LCOE. It is important to research the PID process to understand the underlying mechanisms. This way, PID-proof PV modules can be produced. To detect PID, the PV modules are characterized. The characterization is achieved with the use of light and dark IV measurements, as well as EQE measurements and EL images.

In this thesis, the focus lies on the automation of the time-consuming PID measurements, reducing the labour time. This is achieved by automating the two most time-consuming operations in this process: (i) intermediate PV module characterization and (ii) processing of the acquired data. For the first part, a switch matrix setup is made to stress samples and automatically measure the dark IV curve *in-situ*. This was achieved by designing and implementing the switch matrix and a custom-made LabVIEW program. The program controls the settings of the K2400, which is used for the dark IV measurements, and the settings of the HV-source, used for stressing. For the second part, a custom-made Python program is made to automatically post-process the data. The measurements are assembled in one Excel file. With the use of graphs, the data is visualized. The EL images are first transformed to remove black borders, and then they are combined into one image. Finally, a method is found to calculate the power at STC from the dark IV measurements at stress temperature.

In order to verify the correct operation of the self-developed tools, accelerated PID tests were conducted on five single-cell PV modules. These samples are stressed with the switch matrix setup. The dark IV characteristics were measured every 15 minutes. At certain moments, light IV measurements were conducted with the pv-tools LOANA, and EL images were taken. The data from the switch matrix, LOANA and EL camera were post-processed with the custom-made Python program. It was observed that the samples suffer from PID-s after stressing. To test the inverted mode of the switch matrix, the samples were then cured. After curing, the PID of the samples decreased. The method to calculate the power at STC from the dark IV measurements at stress temperature was verified. The difference between the calculated and actual power is negligible.

The switch matrix setup successfully induced PID in the stressed samples. Therefore, it can be concluded that the custom-made LabVIEW software correctly controls the HV-source, switch matrix and K2400. On top of the basic requirements set by ESE, the tool is also able to reverse PID stress *in-situ* while the characterization continues. Furthermore, the Python program processed the data correctly, and immediately visualizes it with the use of graphs and tables.

Bibliography / References

[1] M. Köntges, S. Kurtz, C. Packard, U. Jahn, K. A. Berger, K. Kato, T. Friesen, H. Liu and M. Van Iseghem, "Review of Failures of Photovoltaic Modules," in *Performance and Reliability of Photovoltaic Systems*, 2014.

[2] Emis, "alternative-energy-tutorials.com," alternative energy tutorials, [Online]. Available: http://www.alternative-energy-tutorials.com/solar-power/photovoltaics.html. [Accessed 06 December 2018].

[3] P. Rahmanpou, S. Saelid and M. Hovd, "Run-To-Run control of the Czochralski process," Elsevier, Norway, 2017.

[4] Sharp Corporation, Japan, "Advances in crystalline silicon solar cell technology for industrial mass production," *npg asia materials,* vol. 2, no. 3, pp. 96-102, july 2010.

[5] A. Sendy, "Pros and Cons of Monocrystalline vs Polycrystalline solar panels," 8 august 2017. [Online]. Available: https://www.solarreviews.com/blog/pros-and-cons-of-monocrystalline-vs-polycrystalline-solar-panels. [Accessed 3 march 2019].

[6] PVEducation, "Multi Crystalline Silicon," [Online]. Available: https://www.pveducation.org/pvcdrom/manufacturing-si-cells/multi-crystalline-silicon. [Accessed 3 March 2019].

[7] J. Liu, Y. Yao, S. Xiao and X. Gu, "Review of status developments of high-efficiency crystalline silicon solar cells," *Journal of Physics D: Applied Physiscs,* vol. 51, p. 12, 2018.

[8] K. O. Davis, M. P. Rodgers, G. Scardera, P. R. Brooker, H. Seigneur, N. Mohajeri, N. G. Dhere, J. Wohlgemuth, E. Schneller, N. Shiradkar, A. C. Rudack and W. V. Schoenfeld, "Manufacturing metrology for c-Si module reliability and durability Part II: Cell manufacturing," *Renewable and Sustainable Energy Reviews,* vol. 59, pp. 225-252, 2016.

[9] R. S. Bonilla and P. R. Wilshaw, "Stable field effect surface passivation of n-type Cz silicon," Elsevier, Department of Materials, University of Oxford, Parks Road, Oxford, United kingdom, 2013.

[10] S. W. Glunz and F. Feldmann, "SiO2 surface passivation layers – a key technology for silicon solar cells," *Solar Energy Materials and Solar Cells,* vol. 185, pp. 260-269, 2018.

[11] R. Guerrero-Lemus, R. Vega, T. Kim, A. Kimm and L. Shephard, "Bifacial solar photovoltaics - A technology review," *Renewable and Sustainable Energy Reviews,* vol. 60, pp. 1533-1549, 2016.

[12] X. Sun, M. R. Khan, C. Deline and M. A. Alam, "Optimization and performance of bifacial solar modules: A global perspective," *Applied Energy,* vol. 212, pp. 1601-1610, 2018.

[13] T. S. Liang, M. Pravettoni, C. Deline, J. S. Stein, R. Kopecek, J. P. Singh, W. Luo, Y. Wang, A. G. Aberle and Y. S. Khoo, "A review of crystalline silicon bifacial photovoltaic performance characterisation and simulation," *Energy & Environmental Science,* vol. 12, pp. 116-148, 2019.

[14] T. Dullweber, H. Schulte-Huxel, S. Blankemeyer, H. Hannebauer, S. Schimanke, U. Baumann, R. Witteck, R. Peibst, M. Köntges, R. Brendel and Y. Yao, "Present status and future perspectives of bifacial PERC+ solar cells and modules," *Japanese Journal of Applied Physics,* vol. 57, p. 9, 2018.

[15] F. Fertig, S. Nold, N. Wöhrle, J. Greulich, I. Hädrich, K. Karin, M. Mittag, D. Biro, S. Rein and R. Preu, "Economic feasibility of bifacial silicon solar cells," *Progress in Phogovoltaics,* vol. 24, pp. 800-817, 2016.

[16] E. J. Schneller, R. P. Brooker, N. S. Shiradkar, M. P. Rodgers, N. G. Dhere, K. O. Davis, H. P. Seigneur, N. Mohajeri, J. Wohlgemuth, G. Scardera, A. C. Rudack and W. V. Schoenfeld, "Manufacturing metrology for c-Si module reliability and durability Part III: Module manufacturing," *Renewable and Sustainable Energy Reviews,* vol. 59, pp. 992-1016, 2016.

[17] K. Zeb, W. Uddin, M. A. Khan, Z. Ali, M. U. Ali, N. Christofides and H. J. Kim, "A comprehensive review on inverter topologies and control strategies for grid connected

photovoltaic system," *Renewable and Sustainable Energy Reviews,* vol. 94, pp. 1120-1141, 2018.

[18] A. R. Jordehi, "Parameter estimation of solar photovoltaic (PV) cells: A review," *Renewable and Sustainable Energy Reviews,* vol. 61, pp. 354-371, 2016.

[19] V. Franzitta, A. Orioli and A. D. Gangi, "Assessment of the Usability and Accuracy of Two-Diode Models for Photovoltaic Modules," *Energies,* vol. 10, pp. 564-595, 2017.

[20] M. Köntges, S. Kurtz, C. Packard, U. Jahn, K. A. Berger, K. Kato, T. Friesen, H. Liu and M. Van Iseghem, "Review of Failures of Photovoltaic Modules," 2014.

[21] D. Cotfas, P. Cotfas and S. Kaplanis, "Methods to determine the dc parameters of solar cells: A critical review," *Renewable and Sustainable Energy Reviews,* vol. 28, pp. 588-596, 2013.

[22] B. Du, R. Yang, Y. He, F. Wang and S. Huang, "Nondestructive inspection, testing, and evaluation for Si-based, thin film and multi-junction solar cells: An overview," *Renewable and Sustainable Energy Reviews,* vol. 78, pp. 1117-1151, 2017.

[23] "What is the best way to calculate series resistance (Rs) and shunt resistance (Rsh) for PV Panels?," Researchgate, 5 May 2016. [Online]. Available: https://www.researchgate.net/post/What_is_the_best_way_to_calculate_series_resistance_Rs_and_shunt_resistance_Rsh_for_PV_Panels. [Accessed 15 May 2019].

[24] V. Naumann, "PID testing of solar cells," Fraunhofer-Center für Silizium-Photovoltaik CSP.

[25] "PVEducation.org," 2018. [Online]. Available: https://pveducation.org/pvcdrom/characterisation/dark-iv-testing. [Accessed 19 November 2018].

[26] D. L. King, B. R. Hansen, J. A. Kratochvil and M. A. Quintana, "Dark current-voltage measurements on photovoltaic modules as a giagnostic or manufacturing tool," in *Conference Record of the Twenty Sixth IEEE Photovoltaic Specialists Conference*, Sandia National Laboratories, Albuquerque, NM, 1997.

[27] D.-M. Tsai, S.-C. Wu and W.-C. Li, "Defect detection of solar cells in electroluminescence images using Fourier image reconstruction," *Solar Energy Materials & Solar Cells,* vol. 99, pp. 250-262, 2012.

[28] V. Nauman, T. Geppert, S. Grober, D. Wichmann, H.-J. Krokoszinski, M. Werner and C. Hagendorf, "Potential-induced degradation at interdigitated back contact solar," in *4th International Conference on Silicon Photovoltaics, SiliconPV 2014*, Fraunhofer Center for Silicon Photovoltaics CSP, Otto-Eißfeldt-Straße 12, 06120 Halle (Saale), Germany , 2014.

[29] J. Melskens, S. Heirmand, R. Koornneef, M. Elshinawy and M. Schouten, "Fast Optical Measurement System: Ultrafast external quantum efficiency," *Solar Energy Materials and Solar Cells,* no. 173, pp. 6-11, 2017.

[30] B. Talukdar, S. Baragohain, S. Kumar, V. Umakanth, N. Sarmah and S. Mahapatra, "Effect of spectral response of solar cells on the module output when individual cells are shaded," *Solar Energy,* vol. 137, pp. 303-307, 2016.

[31] J. Melskens, S. Heirmand, R. Koornneef, M. Elshinawy and M. Schouten, "Fast Optical Measurement System: Ultrafast external quantum efficiency," *Solar Energy Materials and Solar Cells,* vol. 173, pp. 6-11, 2017.

[32] W. Luo, y. s. Khoo, P. Hacke, V. Naumann, D. Laush, S. P. Harvey, J. P. Singh, J. Chai, Y. Wang, A. G. Aberle and S. Ramakrishna, "Potential-induced degradation in photovoltaic modules: a critical review," *Energy & Environmental Science,* vol. 10, no. 43, pp. 43-68, 2017.

[33] J. Carolus, W. De Ceuninck and M. Daenen, "Irreversible damage at high levels of potential-induced degradation on photovoltaic modules," Hasselt, Belgium, 2017.

[34] V. Naumann, D. Lausch, A. Hähnel, J. Bauer, O. Breitenstein, A. Graff, M. Werner, S. Swatek, S. Groser, J. Bagdahn and C. Hagendorf, "Explanation of potential-induced degradation of the shunting type by Na decoration of stacking faults in Si solar cells," *Solar Energy Materials & Solar Cells,* vol. 120, pp. 383-389, 2014.

[35] S. Jonai and A. Masuda, "Origin of Na causing potential-induced degradation for p-type crystalline Si photovoltaic modules," *AIP Advances,* vol. 8, 2018.

[36] V. Naumann, C. Brzuska, M. Werner, S. Grober and C. Hagendorf, "Investigations on the formation of stacking fault-like PID-shunts," Elsevier Ltd., Otto-Eißfeldt-Straße 12, 06120 Halle (Saale), Germany , 2016.

[37] V. Naumann, D. Lausch, A. Hähnel, O. Breitenstein and C. Hagendorf, "Nanoscopic studies of 2D-extended defects in silicon that cause shunting of Si-solar cells," *Physica Status Solidi,* vol. 12, no. 8, pp. 1103-1107, 2015.

[38] J. Slamberger, M. Schwark, B. B. Van Aken and P. Virtic, "Comparison of potential-induced degradation (PID) of n-type ad p-type silicon solar cells," *Energy,* vol. 161, pp. 266-276, 2018.

[39] K. Hara, K. Ogawa, Y. Okabayashi, H. Matsuzaki and A. Masuda, "Influence of surface structure of n-type single-crystalline Si solar cells on potential-induced degradation," *Solar Energy Materials & Solar Cells,* no. 166, pp. 132-139, 2017.

[40] J. Li, Y.-C. Shen, P. Hacke and M. Kempe, "Electrochemical mechanisms of leakage-current-enhanced delamination and corrosion in Si photovoltaic modules," *Solar Energy Materials and Solar Cells,* vol. 188, pp. 273-279, 2018.

[41] P. Hacke, M. Kempe, J. Wohlgemuth, J. Li and Y.-C. Shen, "Potential-Induced Degradation-Delamination Mode in Crystalline Silicon Modules," in *Workshop on Crystalline Silicon Solar Cells and Modules: Materials and Processes*, Vail, Colorado, 2016.

[42] IEC, "IEC 62804 TS: Test methods for detection of potential-induced degradation of crystalline silicon photovoltaic (PV) modules," IEC, 2014.

[43] D. Lausch, V. Naumann, O. Breitenstein, J. Bauer, A. Graff, J. Bagdahn and C. Hagendorf, "Potential-Induced Degradation (PID): Introduction of a Novel Test Approach and Explanation of Increased Depletion Region Recombination," *IEEE Jornal of Photovoltaics,* vol. 4, no. 3, pp. 834-840, 2014.

[44] International Electrotechnical Commission, International Electrotechnical Commission, 2019. [Online]. Available: https://webstore.iec.ch/searchform&q=pv#. [Accessed 23 May 2019].

[45] M. Alonso-Garcia, O. Marin, F. Chenlo and M. Munoz-Garcia, "Characterization of thin film PV modules under standard test conditions: Results of indoor and outdoor measurements and the effects of sunlight exposure," *Solar Energy,* vol. 86, pp. 3049-3056, 2012.

[46] J. Carolus, J. A. Tsanakas, A. van der Heide, E. Voroshazi, W. De Ceuninck and M. Daenen, "Physics of potential-induced degradation in bifacial p-PERC solar cells," *Solar Energy Materials and Solar Cells,* vol. 200, p. 6, 2019.

[47] K. Hara, S. Jonai and A. Masuda, "Potential-induced degradation in photovoltaic modules based on n-type single crystalline Si solar cells," *Solar Energy Materials & Solar Cells,* vol. 140, pp. 361-365, 2015.

[48] W. Oh, S. Bae, D. Kim and N. Park, "Initial detection of potential-induced degradation using dark I-V characteristics of crystalline silicon photovoltaic modules in the outdoors," *Microelectronics reliability,* vol. 88, no. 90, pp. 998-1002, 2018.

[49] W. Luo, P. Hacke, J. P. Singh, J. Chai, Y. Wang, S. Ramakrishna, A. G. Aberle and Y. S. Khoo, "In-Situ Characterization of Potential-Induced Degradation in Crystalline Silicon Photovoltaic Modules Through Dark I-V Measurements," *IEEE Journal of Photovoltaics,* vol. 7, no. 1, 2016.

[50] S. h. Lim, J.-J. Li, E. H. Steenbergen and Y.-H. Zhang, "Luminescence coupling effects on multijunction solarcell external quantum efficiency measurement," *Progress in Photovoltaics: reasearch and application,* no. 21, pp. 344-350, 2013.

[51] pveducation, "pveducation," [Online]. Available: https://www.pveducation.org/pvcdrom/solar-cell-operation/quantum-efficiency. [Accessed 24 Februari 2019].

[52] S. Yamaguchi, A. Masuda and K. Ohdaira, "Changes in the current density–voltage and external quantum efficiency characteristics of n-type single-crystalline silicon photovoltaic modules with a rear-side emitter undergoing potential-induced degradation," *Solar Energy Materials & Solar Cells,* no. 151, pp. 113-119, 2016.

[53] V. Naumann, D. Lausch, S. Groser, M. Werner, S. Swatek, C. Hagendorf and J. Bagdahn, "Microstructural Analysis of Crystal Defects Leading to Potential-Induced Degradation (PID) of Si Solar Cells," *Energy Procedia,* vol. 33, pp. 76-83, 2013.

[54] T. Kawamura, Y. S. Khoo, T. Zhao, Y. Wang and A. G. Aberle, "Quantitative analysis of relationship between leakage current and power loss of multi-crystalline silicon photovoltaic module during potential-induced degradation test," *Japanese journal of applied physics,* vol. 12, no. 56, p. 122301, 2017.

[55] M. Koehl and S. Hoffmann, "Impact of rain and soiling on potential induceddegradation," *PROGRESS IN PHOTOVOLTAICS,* pp. 1304-1309, 2016.

[56] V. Naumann, D. Lausch, K. Ilse, O. Breitenstein, J. Bauer, S. Großer, J. Bagdahn and C. Hagendorf, PID-shunting: Understanding from nanoscale to module level, 2014.

[57] D. Lausch, V. Naumann, A. Graff, A. H¨hnel, O. Breitenstein, C. Hagendorf and J. Bagdahn, "Sodium outdiffusion from stacking faults as root cause for the recovery process of potential-induced degradation (PID)," *Energy Procedia,* vol. 55, pp. 486-493, 2014.

[58] W. Luo, P. Hacke, S. M. Hsian, Y. Wang, A. G. Aberle, S. Ramakrishna and Y. S. Khoo, "Investigation of the Impact of Illumination on the Polarization-Type Potential-Induced Degradation of Crystalline Silicon Photovoltaic Modules," *IEEE Journal of Photovoltaics,* vol. 8, no. 5, pp. 1168-1173, 2018.

[59] "What is LabVIEW?," electronics-notes, [Online]. Available: https://www.electronics-notes.com/articles/test-methods/labview/what-is-labview.php. [Accessed 3 May 2019].

[60] "General Python FAQ," Python Software Foundation, 4 May 2019. [Online]. Available: https://docs.python.org/3/faq/general.html#what-is-python. [Accessed 4 May 2019].

[61] "pv-tools - Model LOANA - Solar Cell Analysis System," Pv-tools, [Online]. Available: https://www.energy-xprt.com/products/pv-tools-model-loana-solar-cell-analysis-system-176627. [Accessed 30 April 2019].

[62] PV-tools, "IQE-SCAN Spectral quantum efficiency & reflectance," PV tools, [Online]. Available: http://www.pv-tools.de/products/iqe-scan.html. [Accessed 30 May 2019].

[63] "D5500," Nikon, [Online]. Available: https://www.nikon.co.uk/en_GB/product/discontinued/digital-cameras/2018/d5500#tech_specs. [Accessed 10 May 2019].

[64] Tektronix, "Series 2400 SourceMeter SMU Instruments," Tektronix, 12 October 2018. [Online]. Available: https://www.tek.com/datasheet/series-2400-sourcemeter-Instruments. [Accessed 16 May 2019].

[65] Tektronix, "Keithley 2400 SourceMeter SMU Instruments," Tektronix, [Online]. Available: https://www.tek.com/keithley-source-measure-units/keithley-smu-2400-series-sourcemeter. [Accessed 13 May 2019].

[66] "Model KB 53," Binder, [Online]. Available: https://www.binder-world.com/en/products/cooling-incubators/series-kb/kb-53. [Accessed 10 May 2019].

[67] MEDER electronic, "H series high voltage reed relays datasheet," [Online]. Available: http://www.farnell.com/datasheets/1523849.pdf?_ga=2.2653424.1931026925.1556520983-1484845059.1539866205. [Accessed 30 april 2019].